



HAL
open science

Quantifying Thermal Infra-Red directional anisotropy using Master and Landsat-8 simultaneous acquisitions

Julien Michel, Olivier Hagolle, Simon J Hook, Jean-Louis Roujean, Philippe Gamet

► **To cite this version:**

Julien Michel, Olivier Hagolle, Simon J Hook, Jean-Louis Roujean, Philippe Gamet. Quantifying Thermal Infra-Red directional anisotropy using Master and Landsat-8 simultaneous acquisitions. Remote Sensing of Environment, 2023, 297, pp.113765. 10.1016/j.rse.2023.113765 . hal-04073733v3

HAL Id: hal-04073733

<https://hal.science/hal-04073733v3>

Submitted on 2 Aug 2023

HAL is a multi-disciplinary open access archive for the deposit and dissemination of scientific research documents, whether they are published or not. The documents may come from teaching and research institutions in France or abroad, or from public or private research centers.

L'archive ouverte pluridisciplinaire **HAL**, est destinée au dépôt et à la diffusion de documents scientifiques de niveau recherche, publiés ou non, émanant des établissements d'enseignement et de recherche français ou étrangers, des laboratoires publics ou privés.



Distributed under a Creative Commons Attribution - ShareAlike 4.0 International License

Quantifying Thermal Infra-Red directional anisotropy using Master and Landsat-8 simultaneous acquisitions

Julien Michel^{a,*}, Olivier Hagolle^a, Simon J. Hook^b, Jean-Louis Roujean^a, Philippe Gamet^a

^a*CESBIO, Université de Toulouse, CNES, CNRS, INRAE, IRD, UT3, 18 avenue Edouard Belin, BPI 2801, TOULOUSE Cedex 9, 31401, France*

^b*Jet Propulsion Laboratory, California Institute of Technology, 4800 Oak Grove Drive, Pasadena, CA 91109, United States*

Abstract

Satellite observations in the Thermal Infra-Red (TIR) domain provide valuable information on Land Surface Temperatures, Evapo-Transpiration and water use efficiency and are useful for monitoring vegetation health, agricultural practices and urban planning. By 2030, there will be 3 new high-resolution global coverage satellite TIR missions in space, all of them with fields of view larger than $\pm 30^\circ$. Directional anisotropy in TIR can affect the estimation of key application variables, such as temperature, and are typically studied by means of field campaigns or physical modelling. In this work, we have evaluated directional effects using simultaneous measurements from Landsat-8 and the $\pm 45^\circ$ field of view MASTER airborne TIR sensor from NASA. Differences as high as 6K are observed in the surface temperatures derived from these simultaneous observations. Those differences are attributed to directional effects, with the greatest differences associated with hotspot conditions, where the solar and satellite viewing directions align. Five well studied parametric directional models have then been fitted to the temperature differences, allowing the amplitude of the measured directional effects to be reduced below 1K, with small variations between models. These results suggest that a simple correction for directional effects could be implemented as part of the ground segment processing for the upcoming missions.

Keywords: Thermal Infra-Red, Land Surface Temperature, MASTER, Landsat-8, Calibration, Anisotropy

*Corresponding author

Email addresses: julien.michel@cnes.fr (Julien Michel), olivier.hagolle@cnes.fr (Olivier Hagolle), simon.j.hook@jpl.nasa.gov (Simon J. Hook), jean-louis.roujean@univ-tlse3.fr (Jean-Louis Roujean), philippe.gamet@cnes.fr (Philippe Gamet)

August 1, 2023

8 **1. Introduction**

9 Earth observation from satellites provide radiometric data in the Thermal InfraRed
10 (TIR) spectrum, namely in the 8-12 μm range, that further serve to estimate the Land
11 Surface Temperature (LST), which is an Essential Climate Variable (ECV). LST is
12 used in a broad range of applications, notably to estimate the surface energy balance
13 (Anderson et al., 2008), and the evapo-transpiration (ET) (Price, 1982; Courault et al.,
14 2005; Anderson et al., 2012), allowing to detect plant water stress (Boulet et al., 2015)
15 and to monitor irrigation (Ishimwe et al., 2014).

16 A new generation of TIR sensors is foreseen to be launched in the coming years.
17 They will have a high spatial resolution (ground sampling distance close to 60 meters
18 at Nadir), and enhanced temporal resolution (every 3 days at equator, and even less at
19 higher latitudes), and between 4 and 5 TIR channels, as well as other optical channels.
20 Table 1 displays the main characteristics of these missions. The first on the agenda is
21 TRISHNA (Thermal infraRed Imaging Satellite for High-resolution Natural resource
22 Assessment) (Lagouarde et al., 2018), scheduled to be launched in 2026. This is a
23 joint Indian and French mission developed by ISRO and CNES. It should be followed
24 in 2027 by the Surface Biology and Geology (SBG) (Cawse-Nicholson et al., 2021),
25 which is a joint mission between NASA and the Italian Space Agency (ASI). Last, the
26 Land Surface Temperature Mission (LSTM) (Koetz et al., 2018) from the European
27 Space Agency will be launched in 2029 for the first satellite and 2030 for the second
28 one. All sensors from these TIR missions will be equipped with large Fields of View
29 (FOV), in order to achieve both global coverage and short revisit time.

30 With maximum zenith angles reaching 30 to 40 degrees, it is expected that direc-
31 tional effects will affect the thermal images and the retrieval of LST by several Kelvins.
32 They could therefore jeopardize the detection and monitoring of water stress as well
33 as other downstream products (Mwangi et al., 2022). A normalization effort seems
34 mandatory in order to reach the target accuracy of 1K for LST. For instance, the hotspot
35 phenomena later introduced in section 1.1 will frequently contaminate TRISHNA, SBG
36 and LSTM scenes in the tropics due to their overpassing time at noon. It is worth em-
37 phasizing that thanks to its orbit design, TRISHNA will provide a workaround to this

38 problem by observing the same scene with at least 3 different viewing angles within
 39 8 days, whereas SBG and LSTM have opted for constant angles. In all cases, pre-
 40 processing of the Level 2 products should benefit from a correction of the directional
 41 effects. It is noteworthy that even if viewing angles of a single are constant for a given
 42 location, directional effects correction may still be required for the joint use of data
 43 from the three missions.

Satellite	Status	Agencies	Launch	Resolution	Revisit	FoV
ASTER	End of life	JAXA	1999	90 .	16 days	8.55°
Landsat-8 & 9	Flying	NASA	2013/21	100 m	8d (2 sat)	7.5°
ECOSTRESS		NASA	2018	38x69 m	irregular	28°
TRISHNA	In prep.	CNES & ISRO	2025	57 m	3d (1 sat)	34°
SBG		NASA	2027	60 m	<8d (1 sat)	34°
LSTM		ESA	2029/31	37 m	2d (2 sat)	28°

Table 1: Main features of high resolution TIR satellites. For missions with two satellites (2 sat), both launch years are mentioned.

44 1.1. Directional anisotropy in the TIR domain

45 Satellite measurements of the LST inherently averages the temperature of visible
 46 elements within a pixel (Li et al., 2013). TIR directional effects are induced by changes
 47 in the proportions of those elements, within a pixel observed from different viewing an-
 48 gles. In structured landscapes, those elements can be divided into sunlit elements and
 49 shaded elements: when the sun and viewing directions get closer, proportion of visible
 50 shaded elements decreases, resulting in a larger proportion of hotter sunlit elements be-
 51 ing observed. This artificially increases the observed temperature, forming the hotspot
 52 phenomenon (Jupp and Strahler, 1991). Another effect inducing TIR anisotropy is the
 53 gap fraction (Nilson, 1999), resulting from the change in proportions of elements with
 54 different emissivities, and thus different temperatures, under the same solar radiation.
 55 For instance, when observing a cropland, observations with large viewing angles will
 56 increase the proportion of vegetation observed, while at nadir, the proportion of soil ob-
 57 served will be higher. In general, for vegetation pixels such as canopies or croplands,

58 the gap fraction and hotspot effects result from the continuous change of proportions
59 of sunlit and shaded leaves and sunlit and shaded background elements, which were
60 modeled as a base shape kernel and a hotspot kernel, respectively, in [Cao et al. \(2021\)](#).
61 More structured landscapes such as rows in croplands can emphasise both the hotspot
62 and gap fraction effects, depending on the row orientation with respect to the satel-
63 lite azimuth ([Lagouarde et al., 2014](#)). Finally, It is noteworthy that directional effects
64 may also affect the Land Surface Emissivity (LSE) ([Sobrino and Cuenca, 1999](#); [Ermida
65 et al., 2020](#)).

66 Directional effects in the reflective domain have been well studied ([Roujean et al.,
67 1992](#); [Wanner et al., 1995](#); [Roujean, 2000](#)) and model-based corrections are routinely
68 applied to high resolution imagery such as Landsat and Sentinel-2 ([Claverie et al.,
69 2018](#)). Directional effects in TIR domain were primarily investigated by means of
70 simulations ([Duffour et al., 2016](#); [Cao et al., 2019](#); [Bian et al., 2020, 2023](#)) using
71 physically-based radiative transfer codes such as 1D SCOPE ([Yang et al., 2021](#)) and 3D
72 DART ([Gastellu-Etchegorry, 1996](#); [Gastellu-Etchegorry et al., 2017](#)). Detailed DART
73 mock-ups were built for various land-cover types. Parametric models ([Ermida et al.,
74 2018](#); [Cao et al., 2021](#)), are considered as the only mean to routinely correct for direc-
75 tional effects, and thereby be used in the ground segments processors. They were eval-
76 uated against SCOPE and DART simulations ([Pinheiro et al., 2006](#); [Bian et al., 2018](#);
77 [Cao et al., 2019](#)), or by cross-comparison with field measurements([Duffour et al., 2016](#))
78 and medium resolution LEO (Low Elevation Orbit) and GEO (geostationary) satellites
79 with large FOVs ([Vinnikov et al., 2012](#); [Guillevic et al., 2013](#); [Ren et al., 2014](#)).

80 Current operating TIR High-Resolution (HR, 10 meter to 100 meter) satellite im-
81 agery is acquired by instruments with a narrow FOV, such as Landsat-8 ($\pm 7.5^\circ$) or
82 ASTER ($\pm 8.5^\circ$), where directional effects do not have a significant impact on LST
83 measurements. A noticeable exception is the ECOSTRESS mission flying onboard the
84 International Space Station (ISS) ([Fisher et al., 2020](#)), with its wide FOV ($\pm 30^\circ$).
85 Currently, there is no systematic correction of directional effects in the level 2 data
86 processing of ECOSTRESS ([Hulley and Hook, 2018](#)).

87 *1.2. Main contributions*

88 Simulating directional effects is valuable to understand the underlying physics, and
89 to evaluate parametric models in a controlled environment. Simulations however have
90 a limited variability with respect to the natural landscape that will be observed by a
91 global coverage satellite mission. Databases of in situ measurements also lack suffi-
92 cient diversity as they focus on a few plant species and land-cover types over selected
93 geographic areas. Lower resolution (larger area) pixels from LEO and GEO satellites
94 TIR images are a good complement to theoretical studies and field campaigns but their
95 large pixels may include different types of landscapes whereas forthcoming higher res-
96 olution TIR missions will focus on a finer scale.

97 This work aims to assess a directional error budget in preparation of up-coming
98 high spatial resolution TIR missions by utilizing available Landsat-8 imagery (Roy
99 et al., 2014) combined with near simultaneous observations from the MODIS/ASTER
100 airborne simulator (MASTER) (Hook et al., 2001). Evidences of directional behavior
101 are identified and compared to several well-established directional models from the
102 literature.

103 Landsat-8 is the well-known Earth-observation satellite from the Landsat series,
104 providing a global coverage of the globe with a 16-days revisit since 2013. Landsat-8
105 has a TIR sensor resolution of 100 meters, though level 1 and 2 products further inter-
106 polate LST products to 30 meters. The Landsat-8 FOV is quite narrow, as its maximum
107 View Zenith Angle (VZA) is 7.5° , and LST maps will therefore be considered as ac-
108 quired under near Nadir conditions in this study. MASTER is an airborne sensor jointly
109 developed by Ames Research Center (ARC), Jet Propulsion Laboratory (JPL), and the
110 EROS Data Center to support algorithms development, calibration and validation for
111 the ASTER and MODIS teams. The MASTER instrument has 50 channels in the 0.4
112 - 13 μm range, with 10 bands in the TIR wavelength range, with a large FOV (maxi-
113 mum VZA of 42.5°). It has been regularly flown since 1998, providing more than 658
114 days of acquisition. Spatial resolution ranges from 5 meters to 50 meters depending
115 on the aircraft flight altitude. While Landsat-8 can provide near Nadir observations,
116 MASTER fully covers the spatial resolution and VZA of the up-coming HR TIR mis-
117 sions listed in table 1. Though ECOSTRESS could also be considered, its FOV (28°)

118 does not cover the full FOV of the up-coming missions. Moreover, ECOSTRESS has
119 a very large swath, and a single Landsat-8 scene only covers a fraction of the VZAs of
120 ECOSTRESS. MASTER being an airborne sensor, it covers the full range of VZA in a
121 very narrow swath that fits completely into a Landsat-8 image.

122 The remainder of this paper is organised as follows. Section 2 presents the matching
123 methodology, the data processing, as well as the directional models and models fitting
124 procedure. Section 3 presents LST comparison statistics for each match, the evidences
125 of the directional effects and the performances of directional models fitted on the data.
126 Section 4 discusses the limitations and possible follow-up to this study, and section 5
127 summarizes the results and future work.

128 **2. Materials and methods**

129 *2.1. Matching methodology*

130 The full MASTER archive metadata has been kindly provided by JPL, and Landsat-
131 8 collection 2 level 2 archive metadata (as of 2022.02.17) has been downloaded from
132 the Land Processes DAAC. From these data, all pairs of MASTER and Landsat-8 prod-
133 ucts acquired during day-time, on the same date, with acquisition times within 10 min-
134 utes of each other, and with an overlap of respective bounding boxes no less than 50%
135 have been selected.

136 Using this search process, 52 matches were identified, for which the Landsat-8
137 overpass occurs during MASTER track flight. Those 52 matches correspond to 24
138 unique MASTER tracks since one track can correspond to two Landsat-8 product.
139 Among those 52 matches, 7 MASTER tracks are missing in the archive, which invali-
140 dates 17 pairs. This leaves 35 pairs for which both Landsat-8 products and MASTER
141 L1B (radiance at sensor) and L2 (derived LST and emissivities) products are available.
142 Among those, there are 16 pairs for which the processing described in section 2.2 does
143 not yield a valid difference image, because of cloud occurrences or insufficient swath
144 final overlap. Table 2 gives the products references of all valid pairs used in this study.
145 As shown in figure 1, all sites are located in California or nearby. Figure 2 shows a
146 detailed map view of valid overlapping area for each MASTER track, with the overlap

147 of the second Landsat-8 image in blue when applicable. This map shows that for most
 148 of the tracks (3, 4, 6, 10, 12), the second Landsat-8 does not bring additional coverage,
 149 to the noticeable exception of tracks 8 and 9.

Id	MASTER track id	Landsat L2 product id
1	2013-03-29_18:06:53	LC08_L2SP_038037_20130329_20200912_02_T1
2	2013-04-11_18:14:46	LC08_L2SP_041036_20130411_20200912_02_T1
3a	2013-05-22_18:13:09	LC08_L2SP_040036_20130522_20200913_02_T1
3b	2013-05-22_18:13:09	LC08_L2SP_040037_20130522_20200913_02_T1
4	2013-12-05_18:23:35	LC08_L2SP_043035_20131205_20200912_02_T1
5a	2014-03-31_18:11:16	LC08_L2SP_039035_20140331_20200911_02_T1
5b	2014-03-31_18:11:16	LC08_L2SP_039036_20140331_20200911_02_T1
6a	2014-04-14_18:27:14	LC08_L2SP_041036_20140414_20200911_02_T1
6b	2014-04-14_18:27:14	LC08_L2SP_041037_20140414_20200911_02_T1
7	2014-04-28_18:22:43	LC08_L2SP_043035_20140428_20200911_02_T1
8a	2014-06-06_18:25:35	LC08_L2SP_044033_20140606_20200911_02_T1
8b	2014-06-06_18:25:35	LC08_L2SP_044034_20140606_20200911_02_T1
9a	2014-10-21_18:35:15	LC08_L2SP_043034_20141021_20200910_02_T1
9b	2014-10-21_18:35:15	LC08_L2SP_043035_20141021_20200911_02_T1
10a	2015-05-28_18:13:05	LC08_L2SP_040036_20150528_20200909_02_T1
10b	2015-05-28_18:13:05	LC08_L2SP_040037_20150528_20200909_02_T1
11	2018-06-19_18:28:30	LC08_L2SP_042034_20180619_20200831_02_T1
12a	2021-03-30_18:32:40	LC08_L2SP_043033_20210330_20210409_02_T1
12b	2021-03-30_18:32:40	LC08_L2SP_043034_20210330_20210409_02_T1

Table 2: List of valid MASTER and Landsat-8 pairs

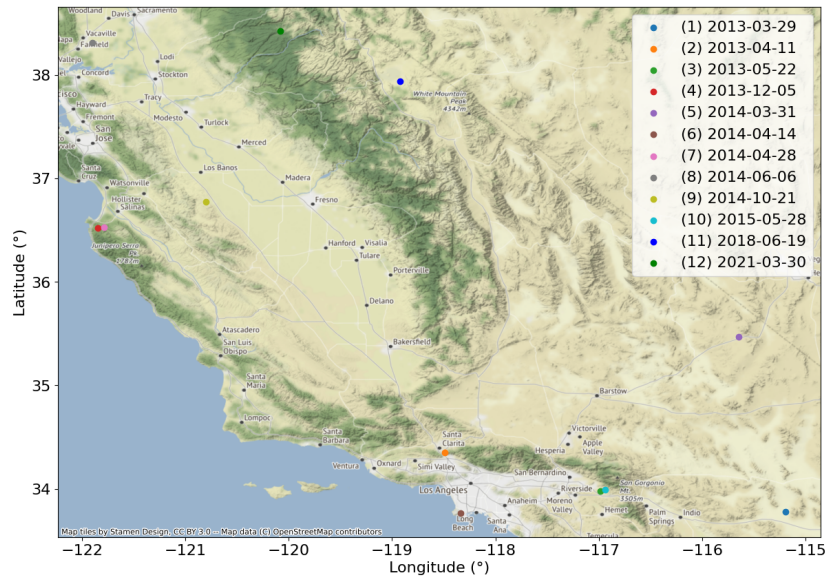


Figure 1: Location of the 12 MASTER tracks that have been matched to near simultaneous Landsat-8 acquisitions

150 *2.2. Data Processing*

151 *2.2.1. Product downloads*

152 Landsat-8 products have been downloaded from the collection 2 level 2 archive
 153 from the EarthExplorer portal¹. MASTER L1B products (radiances and viewing an-
 154 gles), as well as L2 products (LST and geo-location grids) have been requested on
 155 the MASTER website². Landsat-8 viewing angles have been computed by using a C
 156 program publicly available on USGS website³.

157 *2.2.2. Target variables*

158 *Surface Brightness Temperature (SBT)*. Both mission output LST and LSE maps. But
 159 they differ in the way those variables are estimated. On Landsat-8, there is a single

¹<https://earthexplorer.usgs.gov/>, consulted on 2023.03.01

²<https://masterprojects.jpl.nasa.gov/>, consulted on 2023.03.01

³<https://www.usgs.gov/landsat-missions/solar-illumination-and-sensor-viewing-angle-coefficient-file>,
 consulted on 2022.09.12

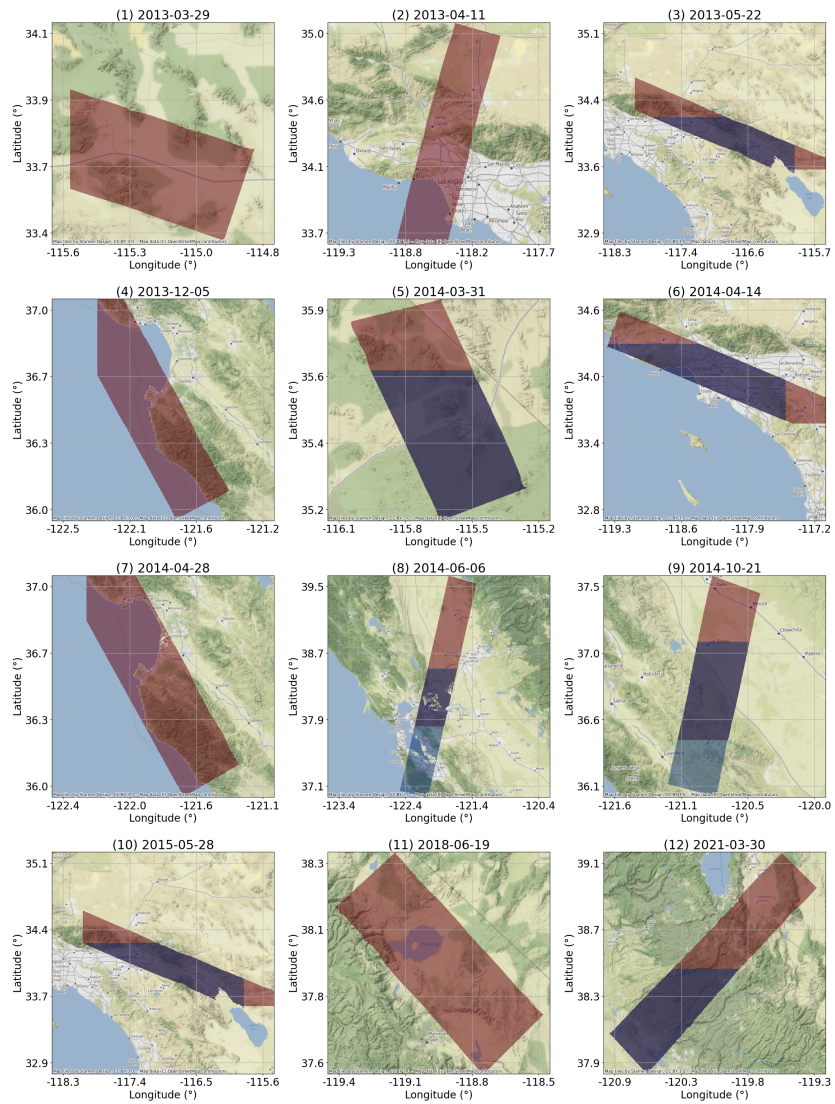


Figure 2: Detailed view of the overlapping MASTER tracks and Landsat-8 near simultaneous acquisitions. When two Landsat-8 images match a given track, the first image (a) is displayed in red and second image (b) in blue.

160 usable TIR band (B10, 10.6 - 11.19 μm), which prevents a joint estimation of LST and
 161 LSE. LSE is therefore derived by modulating the LSE from the ASTER Global Emis-
 162 sivity Database (Hulley et al., 2015) with the Normalized Difference Index (NDVI) and
 163 Snow Difference Index (NDSI) measured by Landsat-8. Various rules are applied to
 164 clamp emissivity values in corner cases. One important thing to note is that any emis-
 165 sivity lower than 0.6 is considered invalid and flagged as missing data. LST is then
 166 obtained by inverting the radiative transfer equation 1, with the atmospheric transmit-
 167 tance, upwelled and downwelled radiance estimated using (MODerate resolution atmo-
 168 spheric TRANsmission (MODTRAN) (Berk et al., 2014), Modern-Era Retrospective
 169 analysis for Research and Applications, Version 2 (MERRA-2) (Gelaro et al., 2017)
 170 and data from the GEOS-5 FP-IT Atmospheric Data Assimilation System (GEOS-5
 171 ADAS) (Malakar et al., 2018).

$$L_\lambda(\theta) = [\epsilon_\lambda B_\lambda(T_s) + (1 - \epsilon_\lambda)L_\lambda^\downarrow]\tau_\lambda(\theta) + L_\lambda^\uparrow(\theta) \quad (1)$$

172 where $L_\lambda(\theta)$ is the at sensor radiance, λ is the wavelength, θ is the observation angle,
 173 ϵ_λ the surface emissivity, T_s is the Surface Temperature, L_λ^\downarrow is the downwelled radiance,
 174 $\tau_\lambda(\theta)$ is the atmospheric transmittance, $L_\lambda^\uparrow(\theta)$ is the upwelled radiance and $B_\lambda(T_s)$ is the
 175 Planck function defined in equation 2.

$$B_\lambda(T_s) = \frac{2hc^2}{\pi\lambda^5 \left(\exp\left(\frac{hc}{\lambda T_s}\right) - 1 \right)} = \frac{C_1}{\lambda^5 \left(\exp\left(\frac{C_2}{\lambda T_s}\right) - 1 \right)} \quad (2)$$

176 Where $h = 6.63 \times 10^{-34} \text{Ws}^2$ (Planck constant), $c = 2.99 \times 10^8 \text{ms}^{-1}$ (speed of light),
 177 $k = 1.38 \times 10^{-23} \text{WsK}^{-1}$ (Boltzmann constant), $C_1 = 2\pi hc^2 = 3.74 \times 10^{-16} \text{Wm}^2$ (first
 178 radiative constant) and $C_2 = hc/k = 1.44 \times 10^4 \mu\text{mK}$ (second radiative constant).

179 MASTER, on the other hand, uses the ASTER TES algorithm to retrieve LST val-
 180 ues (Hook et al., 2011), using MODTRAN radiative transfer code and atmospheric
 181 parameters the Global Data Assimilation System (GDAS) products from the National
 182 Center for Environmental Prediction (NCEP). Those parameters are optimized for a
 183 flight altitude of 20 kilometers. Level 2 products include LST estimates as well emis-
 184 sivity estimates for channels 43, 44, 47, 48 and 49.

185 Since the algorithms for the separation of emissivity and LST are different, those

186 two variables may exhibit differences that are not related to directional effects. In order
 187 to limit the impact of those differences, this study recomputes the Surface Brightness
 188 Temperature (SBT), which corresponds to the temperature of a black-body emitting the
 189 same surface radiance, for both sensors, by means of equation 3, where $\lambda = 10.9\mu m$
 190 (center wavelength of Landsat-8 B10 band).

$$SBT = B_{\lambda}^{-1}(emis * B_{\lambda}(LST)) \quad (3)$$

191 Note that equation 3 is only changing the balance between already estimated emis-
 192 sivities and LST, under the same radiative transfer budget.

Equivalent Landsat-8 emissivity from MASTER. MASTER channels 47 and 48 overlap Landsat-8 B10 spectral sensitivity response, as shown in figure 3. Since the overlaps are significant, an equivalent Landsat-8 B10 emissivity is derived from MASTER, by means of linear combination of emissivities of channel 47 and 48, as shown in equation 4 to 6. The weights of the linear combinations are derived from the integration of the product of spectral sensitivities response, which correspond to the green and orange areas in figure 3. Weights are given in equation 7. This equivalent emissivity will be used as the MASTER emissivity throughout this study.

$$\epsilon^* = \frac{w_{47}}{w_{47} + w_{48}} \epsilon_{47} + \frac{w_{48}}{w_{47} + w_{48}} \epsilon_{48} \quad (4)$$

$$w_{47} = \int_{\lambda} SRS_{B10}^{landsat-8}(\lambda) * SRS_{47}^{MASTER}(\lambda) \quad (5)$$

$$w_{48} = \int_{\lambda} SRS_{B10}^{landsat-8}(\lambda) * SRS_{48}^{MASTER}(\lambda) \quad (6)$$

193

$$\frac{w_{47}}{w_{47} + w_{48}} = 0.605, \quad \frac{w_{48}}{w_{47} + w_{48}} = 0.395 \quad (7)$$

194 2.2.3. Geometric processing

195 In order to compare measurements from products from the different sensors, they
 196 need to be first resampled to a common cartographic sampling grid. For each pair, this
 197 grid is defined using the Universal Transverse Mercator (UTM) cartographic projection
 198 of the Landsat-8 image of the pair. The sampling grid is defined according to the
 199 overlap area of the two products, and aligned to a multiple of the target resolution. The

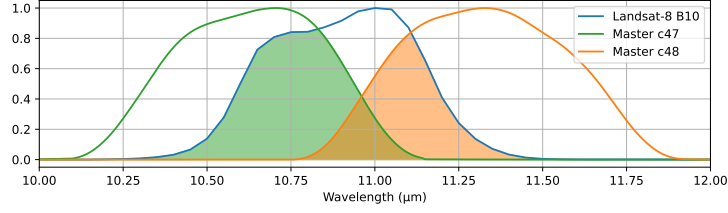


Figure 3: Spectral Sensitivity Response of Landsat-8 and MASTER overlapping Thermal Infra-Red spectral bands

200 target resolution is set to 100 meters for pairs of Landsat-8 and MASTER images, since
 201 the native resolution of Landsat-8 TIR bands is 100 meter.

202 Landsat-8 resampling is achieved through an averaging filter, which should not
 203 incur any aliasing artifacts since the Landsat-8 LST and emissivity measurements are
 204 resampled at 30 meters resolution through bicubic interpolation. MASTER being a
 205 whisk-broom sensor, its sampling is regular in viewing angle and therefore irregular in
 206 ground geometry: both spacing between pixels and pixel size increase with the viewing
 207 angle. Resampling of those measurements to the target ground grid is achieved by
 208 means of Gaussian Weights Averaging (GWA), as described in equation 8, through its
 209 implementation in the *pyresample* library (Hoese et al., 2022):

$$V(x, y) = \sum_{i \in N(x, y)} e^{-\frac{(x-x_i)^2 + (y-y_i)^2}{\sigma^2}} V_i \quad (8)$$

210 Where (V_i, x_i, y_i) are swath samples of measurement V at location (x_i, y_i) , $N(x, y)$
 211 are the N nearest neighbours of target ground location (x, y) , and σ is a user-defined
 212 parameter, which is set using equation 9:

$$\sigma(r, R, mtf) = \frac{\max(r, R)}{\pi} \sqrt{-2 \ln(mtf)} \quad (9)$$

213 Where mtf is the value of the Modulation Transfer Function (MTF) at Nyquist
 214 cut-off frequency, allowing to trade level of blur and aliasing off, r is the native sensor
 215 resolution and R is the target resolution. In this work, MTF has been set to 0.1, which
 216 yields a sigma of 68.3 meters for MASTER.

217 Given that all MASTER flights occurred at an altitude between 19 702 meters and
 218 20 088 meters, depending on the position in the swath and the flight azimuth, the output

219 100 meter pixels cover between 12.5 milliradians and 23.7 milliradians of the initial
 220 instantaneous MASTER FOV, which is 2.25 milliradians per pixel.

221 2.2.4. *Quality filtering*

222 Only samples that are marked as clear and not flagged as water or snow in the Pixel
 223 Quality Assessment mask from the Level 2 Landsat-8 products are kept for analysis.
 224 No additional quality filtering is performed on the MASTER side.

225 2.2.5. *Angular distance*

226 Let (θ_0, ϕ_0) and (θ_1, ϕ_1) denote two viewing directions by their zenith angle θ and
 227 azimuth angle ϕ . The angle between those two viewing directions is given by equation
 228 10:

$$D_{ang}(\theta_0, \phi_0, \theta_1, \phi_1) = \arccos(\sin(\theta_0) \times \sin(\theta_1) \times \cos(\phi_0 - \phi_1) + \cos(\theta_0) \times \cos(\theta_1)) \quad (10)$$

229 This distance is used in this work to measure proximity to hotspot conditions, as
 230 well as to measure distance between MASTER and Landsat-8 viewing directions.

231 2.3. *Directional parametric models*

232 Four models investigated by Cao et al. (2019) have been used in this work: the
 233 Ross-Li model (Roujean et al., 1992; Wanner et al., 1995; Ren et al., 2014), the LSF-Li
 234 model (Su et al., 2002), the Vinnikov model (Vinnikov et al., 2012) and the RL model
 235 (Roujean, 2000; Lagouarde and Irvine, 2008). In addition to those models, we also
 236 investigated the LSF-RL model from Cao et al. (2021). Models are presented in table 3,
 237 where θ_v (resp. θ_s) is the view (resp. solar) zenith angle, and Δ_ϕ denotes the difference
 238 between solar and view azimuth angle. Unless stated otherwise, remaining notations
 239 and kernel expressions will be those from Cao et al. (2019). The full kernel functions
 240 are not provided here for the sake of conciseness. All models m will be expressed as
 241 stated in equation 11, with k_0, \dots, k_n being the free parameters of the model:

$$T(\theta_v, \theta_s, \Delta_\phi) = m(\theta_v, \theta_s, \Delta_\phi, k_0, \dots, k_n) \times T_{Nadir} \quad (11)$$

242 For the sake of consistency with the other models, the Roujean-Lagouarde (RL)
 243 kernel has been rewritten as equation 12:

$$K_{RL}(\theta_v, \theta_s, k_{hs}) = \frac{e^{-k_{hs}f} - e^{-k_{hs}f_n}}{1 - e^{-k_{hs}f_n}} \quad (12)$$

244 with f and f_n as written in Cao et al. (2019) (eq. 13 and 14). This mainly moves
 245 the original Δ_T parameter out of the kernel formulation, in order to use it as a kernel
 246 coefficient in table 3. It must be stressed that the RL model is the only one that does
 247 not have a volumetric kernel, but only a geometric kernel. The LSF-RL complement
 248 the RL model with the LSF volumetric kernel. To make that more obvious, in table 3,
 249 the parameter k_0 always represents the isotropic contribution, while k_1 stands for the
 250 coefficient of the volumetric kernel (and therefore the RL model has no k_1 parameter),
 251 and k_2 is the coefficient of the geometric or hotspot kernel. The hotspot width parameter
 252 inside the exponential in 12 is labelled k_{hs} , and it should be noted that the RL and LSF-
 253 RL models are the only models with parameters non-linearity.

Model	Iso	Volumetric	Geometric / Hotspot
Ross-Li	k_0	$+ k_1 \mathbf{K}_{\text{RossThick}}(\theta_v, \theta_s, \Delta_{\text{phi}})$	$+ k_2 \mathbf{K}_{\text{LiSparseR}}(\theta_v, \theta_s, \Delta_{\text{phi}})$
LSF-Li	k_0	$+ k_1 \mathbf{K}_{\text{lsf}}(\theta_v, \theta_s, \Delta_{\text{phi}})$	$+ k_2 \mathbf{K}_{\text{LiDenseR}}(\theta_v, \theta_s, \Delta_{\text{phi}})$
Vinnikov	k_0	$+ k_1 \mathbf{K}_{\text{emis}}(\theta_v, \theta_s, \Delta_{\text{phi}})$	$+ k_2 \mathbf{K}_{\text{solar}}(\theta_v, \theta_s, \Delta_{\text{phi}})$
RL	k_0		$+ k_2 \mathbf{K}_{\text{RL}}(\theta_v, \theta_s, \Delta_{\text{phi}}, k_{hs})$
LSF-RL	k_0	$+ k_1 \mathbf{K}_{\text{lsf}}(\theta_v, \theta_s, \Delta_{\text{phi}})$	$+ k_2 \mathbf{K}_{\text{RL}}(\theta_v, \theta_s, \Delta_{\text{phi}}, k_{hs})$

Table 3: Formulations of the five directional models from Cao et al. (2019) as well as of the LSF-RL model from Cao et al. (2021) investigated in this work

254 The fitting of model parameters on the data has been performed by ordinary Least-
 255 Squares as stated in equation 13:

$$\min_{(k_0, k_1, k_2, k_{hs})} \| m(\theta_v, \theta_s, \Delta_{\text{phi}}, k_0, \dots, k_{hs}) \times T_{\text{Nadir}} - T_{\text{Dir}}(\theta_v, \theta_s, \Delta_{\phi}) \|^2 \quad (13)$$

256 where Landsat-8 SBT is used as T_{Nadir} and MASTER SBT is used as T_{Dir} . Pa-
 257 rameters k_0 , k_2 and k_{hs} are assumed to be strictly positive, and in Cao et al. (2019)
 258 the authors observe that k_1 is always negative. Additionally, k_{hs} can not equal 0 in or-

259 der to avoid a null denominator in the exponential fraction. In order to enforce those
 260 constraints while still using unconstrained least-squares fitting, the models have been
 261 re-parametrized with exponential, and a small offset of 1e-6 has been added to k_{hs} to
 262 avoid the under-determination around 0, as shown in equation 14:

$$k_0 = e^{k'_0}, \quad k_1 = -e^{k'_1}, \quad k_2 = e^{k'_2}, \quad k_{hs} = 1e - 6 + e^{k'_{hs}} \quad (14)$$

263 Optimization has been performed using the Levenberg-Marquardt algorithm imple-
 264 mented in scipy (Virtanen et al., 2020). Initial values have been set to 1. for k_0 , 0.01
 265 for k_1 and k_2 , which corresponds to a variation of SBT of 1% that is consistent with the
 266 observations in the dataset, and 1 for k_{hs} , where k_0 , k_1 , k_2 and k_{hs} defined in table 3.

267 2.4. Land-cover analysis

268 According to the literature, Land cover is one of the main drivers for TIR direc-
 269 tional anisotropy, as both gap fraction and hotspot effects are driven by the structure of
 270 the landscape, and in particular, of the vegetation. In order to provide insights on the
 271 land-cover classes covered by each of the tracks, five high level classes have been ex-
 272 tracted from the Copernicus Global Land Service maps at 100 meter resolution (Tsend-
 273 bazar et al., 2021). This land cover source has been selected because it is available as
 274 open-data, it covers the area of interest and provides several years of land cover maps
 275 covering the observation period. Maps from Copernicus GLS only cover years 2015
 276 to 2019, whereas MASTER tracks cover years 2013 to 2021, therefore tracks prior to
 277 2015 have been assigned the 2015 land cover, while tracks posterior to 2019 have been
 278 assigned the 2021 land cover, under the assumption that land cover only marginally
 279 changes from one year to another, especially for high level classes. High level classes
 280 are aggregated from the land-cover maps as described in table 4. Furthermore, since
 281 vegetation can be at different stages of growth depending on plant type and season, the
 282 cropland, low vegetation and forests classes have been further stratified according to
 283 the Normalized Difference Vegetation Index (NDVI) (Kriegler et al., 1969) computed
 284 from Landsat-8 in three sub-classes : low NDVI (between 0 and 0.2), intermediate
 285 NDVI (between 0.2 and 0.6), and high NDVI (greater than 0.6).

High level class	Copernicus Global Land Service classes (label)
Urban	Urban / built up (50)
Bare	Bare / sparse vegetation (60)
Croplands	Cultivated and managed vegetation/agriculture (cropland) (40)
Low vegetation	Shrubs (20)
	Herbaceous vegetation (30)
	Herbaceous wetland (90)
	Moss and lichen (100)
Forests	Closed forest, evergreen needle leaf (111)
	Closed forest, evergreen, broad leaf (112)
	Closed forest, deciduous needle leaf (113)
	Closed forest, deciduous broad leaf (114)
	Closed forest, mixed (115)
	Closed forest, unknown (116)
	Open forest, evergreen needle leaf (121)
	Open forest, evergreen broad leaf (122)
	Open forest, deciduous needle leaf (123)
	Open forest, deciduous broad leaf (124)
	Open forest, mixed (125)
	Open forest, unknown (126)

Table 4: The five high level class derived from class aggregation of the Copernicus Global Land Service classes

286 Table 5 gives the proportions of each classes for each analysed MASTER track.
 287 All proportions are given in percentage of the total number of available pixels. In this
 288 table, it can be noted that low vegetation and croplands seldom reach the highest NDVI
 289 strata, while forests have intermediate to high NDVI, which is expected and advocate
 290 for the consistency between the derived land-cover maps and the observed landscapes.
 291 Track (1) is mostly composed of bare soil. Tracks (8) and (9) are the only ones with
 292 a significant proportion of croplands, all in the intermediate NDVI strata. Tracks (2)
 293 and (6) are the only ones with a significant proportion of urban pixels, and are com-
 294 plemented with low to intermediate NDVI classes of low vegetation. Remaining tracks
 295 are a mix of forests with intermediate to high NDVI, and low vegetation with low to
 296 intermediate NDVI.

ndvi	bare	urban	crops			forests			low veg.		
			low	inter	high	low	inter	high	low	inter	high
(1)	80.9	0.1	0.0	0.0	0.0	0.0	0.0	0.0	18.6	0.3	0.0
(2)	1.9	25.2	0.1	0.1	0.1	0.0	3.1	3.0	34.1	29.2	3.2
(3)	16.0	11.9	0.0	0.0	0.0	0.1	15.7	8.6	20.0	26.4	1.1
(4)	0.1	3.9	0.0	0.1	0.0	0.3	26.8	56.8	0.5	9.9	1.4
(5)	17.5	0.0	0.0	0.1	0.2	0.0	0.7	0.0	73.9	7.5	0.0
(6)	0.8	51.0	0.2	2.4	1.0	0.1	5.0	4.8	1.9	29.0	3.8
(7)	0.1	3.1	0.3	3.4	1.5	0.0	15.5	57.0	0.2	13.2	5.4
(8)	0.2	13.4	4.0	28.3	8.7	0.1	10.9	14.4	1.3	17.5	0.7
(9)	0.0	2.2	9.0	26.3	4.3	0.0	6.1	0.8	18.2	32.9	0.1
(10)	20.6	14.5	0.0	0.1	0.0	0.1	13.5	4.7	20.4	25.4	0.6
(11)	14.5	0.0	0.0	0.0	0.0	0.5	23.2	0.9	18.9	39.6	2.3
(12)	0.9	1.0	0.1	0.9	0.3	1.9	28.9	33.4	12.8	14.5	5.2

Table 5: Percentage of land-cover classes for each track. Vegetation classes are further stratified according to Landsat-8 NDVI into [0,0.2] (low), [0.2,0.6] (intermediate) and [0.6, 1.0] (high). Classes exceeding 15% of available pixels are highlighted in bold for the sake of readability.

297 **3. Results**

298 *3.1. SBT difference analysis*

299 Table 6 shows the biases and RMSE of LST and SBT differences (Landsat-8 -
300 MASTER), for each MASTER track, and for samples for which angles between view-
301 ing directions are below 7° . Though each track exhibits an absolute LST bias lower
302 than 1.8 K (1.6 K for SBT), the biases of each track vary significantly within this range.
303 Standard deviation values range from 0.7 K to up to 2.2 K for LST and 0.6K to 2K for
304 SBT, if we exclude track (10) which exhibits a very large standard deviation. Those
305 values are in line with recent Landsat-8 LST performance assessment for Landsat-8
306 Collection 2 Level 2 (Niçlòs et al., 2021). For all tracks, SBT standard deviation is
307 lower than LST standard deviation. SBT is therefore more suitable for the analysis in
308 this paper, as it seems to discard discrepancies related to the different LST - emissivity
309 separation methods detailed in section 2.2.2. In order to further reduce discrepancies
310 unrelated to directional anisotropy, on each track SBT differences will be corrected
311 from the bias, so that similar viewing angles between MASTER and Landsat-8 corre-
312 spond to a null SBT difference on average. It is noteworthy that standard deviation in
313 table 6 corresponds to the Root Mean Squared Error (RMSE) of the de-biased data.

314 Figure 4 shows the SBT difference maps for each track, which have been corrected
315 from the biases shown in table 6. Most tracks exhibit a pattern related to the position
316 in the MASTER swath, and thus to the MASTER VZA. This is for instance the case
317 form tracks (2), (6), (7), (8) and (12), where MASTER SBT appears to be consistently
318 warmer on the western side of the swath than on the eastern side of the swath. Tracks
319 (4), (9) and (10) have the highest SBT difference standard deviations in table 6 and ex-
320 hibit spatial patterns that seem uncorrelated to TIR anisotropy. Inspection of Landsat-8
321 cirrus band B9 in level 1C products from collection 2 reveals that track (10) is heavily
322 contaminated by unmasked cirrus clouds, which explains both its high SBT difference
323 standard deviation and large spatial patterns in SBT difference map. Likewise, a closer
324 inspection of track (4) reveals that the SBT difference map is completely dominated
325 by terrain effects, which explains both its high SBT difference standard-deviation and
326 noisy spatial patterns. Inspection of remaining tracks reveals that track (9) is also partly

Track	#samples	LST		SBT	
		Bias	Std dev	Bias	Std dev
(1) 2013-03-29	5187	-0.6	0.7	-0.7	0.6
(2) 2013-04-11	69125	0.3	1.4	0.6	1.3
(3) 2013-05-22	59011	1.4	1.6	1.1	1.5
(4) 2013-12-05	7409	0.7	1.9	0.4	1.9
(5) 2014-03-31	22037	1.2	1.0	0.9	0.6
(6) 2014-04-14	73182	0.4	1.2	0.2	1.1
(7) 2014-04-28	13012	0.6	1.0	1.0	1.0
(8) 2014-06-06	138921	-0.3	1.8	-0.1	1.7
(9) 2014-10-21	74247	-1.5	2.1	-1.5	2.1
(10) 2015-05-28	97435	-0.1	5.5	-0.3	5.4
(11) 2018-06-19	36706	-1.3	1.7	-1.6	1.6
(12) 2021-03-30	62572	-1.7	1.9	-1.1	1.7

Table 6: Bias and RMSE of Land Surface Temperature and SBT difference (Landsat-8 - MASTER) for samples with an absolute viewing angles distance below 7°

327 contaminated by unmasked cirrus clouds and terrain effects. Tracks (4), (9) and (10)
328 have therefore been excluded from the analysis in the remaining of this paper.

329 *3.2. Directional effects analysis*

330 *3.2.1. Distance to hotspot vs. distance to Landsat-8 viewing direction*

331 In figure 5, SBT differences, corrected from the biases shown in table 6, are anal-
332 ysed with respect to both MASTER view angular distance to hotspot and to Landsat-8
333 viewing direction. All graphs exhibit the same v-shaped curve, which is induced by the
334 relative viewing geometries between Landsat-8 and MASTER. Since Landsat-8 has a
335 narrow FOV, the minimum angular distance between views occurs far from the hotspot
336 condition (usually between 20° and 50° of distance to the hotspot), and with MASTER
337 view close to Nadir. On the left of the minimum point, which corresponds to the west-
338 ern part of the MASTER swath, the MASTER view gets closer to the hotspot, which
339 correlates with MASTER temperature getting hotter than Landsat-8 temperature. This
340 is especially visible for tracks (2), (8) and (12), which are also the tracks that come
341 closer to the hotspot. On the right of the minimum point, which corresponds to the
342 eastern part of the MASTER swath, the view gets away from the hotspot condition,
343 which correlates in most views with MASTER getting colder than Landsat-8. Tracks
344 (1), (3), (5) and (11) will be further analysed in section 3.2.2.

345 *3.2.2. MASTER view zenith and azimuth*

346 Figure 6 allows to better understand the angular configurations of each MASTER
347 track with respect to the position of the sun. Two kinds of configurations can be ob-
348 served. In hotspot conditions, when the sun is close to the principal observation plane,
349 as in tracks (2), (8) and (12), the temperature steadily increases while coming closer to
350 the sun position. On track (8), MASTER view zenith gets higher than the sun zenith
351 which results in a cool-down of the SBT. Track (12) shows that the sun is almost in the
352 principal plane, which explains why this track has the smallest distance to the hotspot.
353 When the sun is far from the principal observation plane however, SBT gets colder
354 with higher view zenith angle, on both ends of the swath. The difference with Landsat-
355 8 SBT comes to a minimum near nadir, but the position of this minimum varies and

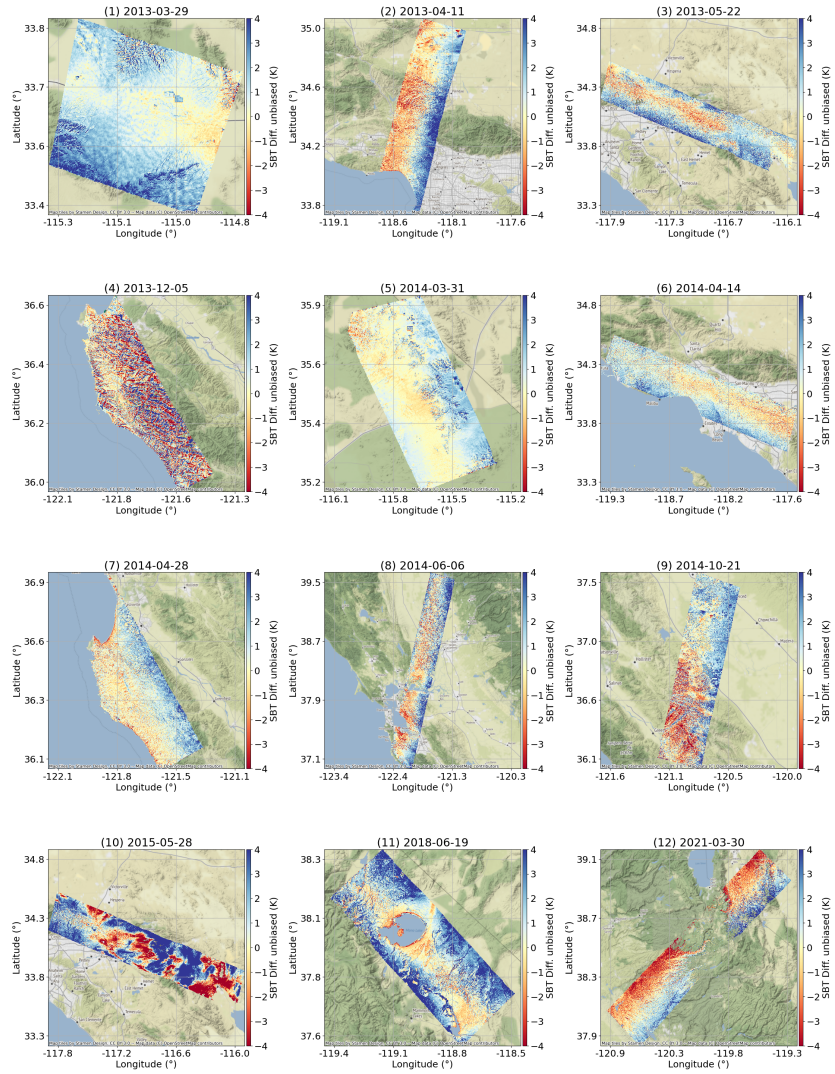


Figure 4: Maps of SBT difference (Landsat-8 - MASTER), corrected of the bias computed in table 6 for all tracks (negative values are in red and mean that MASTER is warmer than Landsat-8)

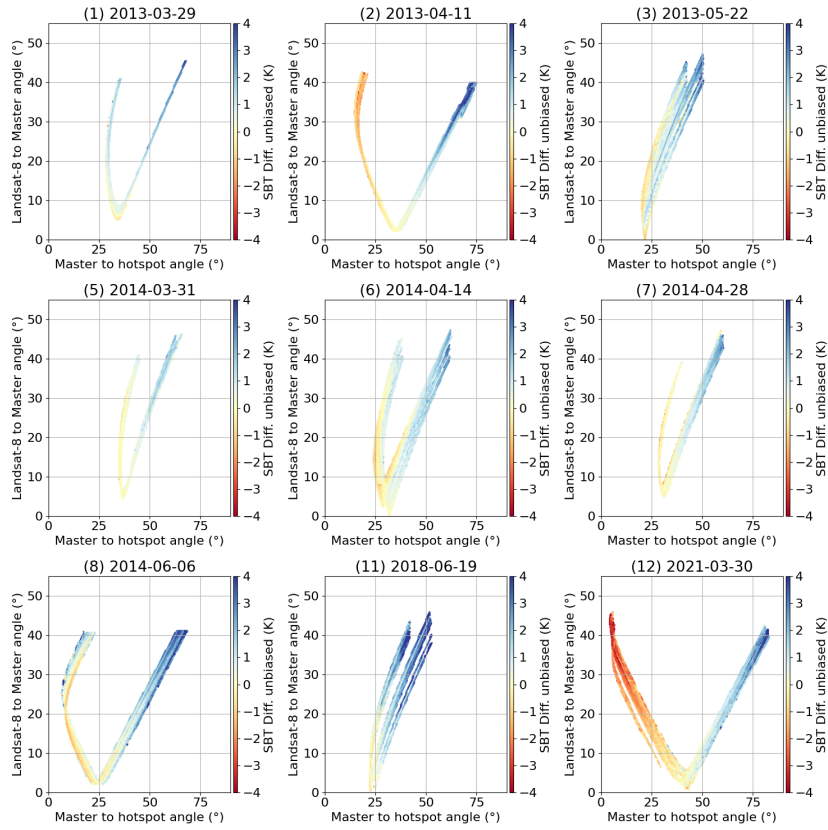


Figure 5: SBT difference (Landsat-8 - MASTER) with respect to angular distance from MASTER to hotspot and from MASTER to Landsat-8, corrected of the bias computed in table 6 (negative values are in red and mean that MASTER is warmer than Landsat-8)

356 seems to be influenced by the position of the sun. This may be related to gap fraction
 357 effect and can be observed on tracks (1), (3), (5), (6), (7) and (11).

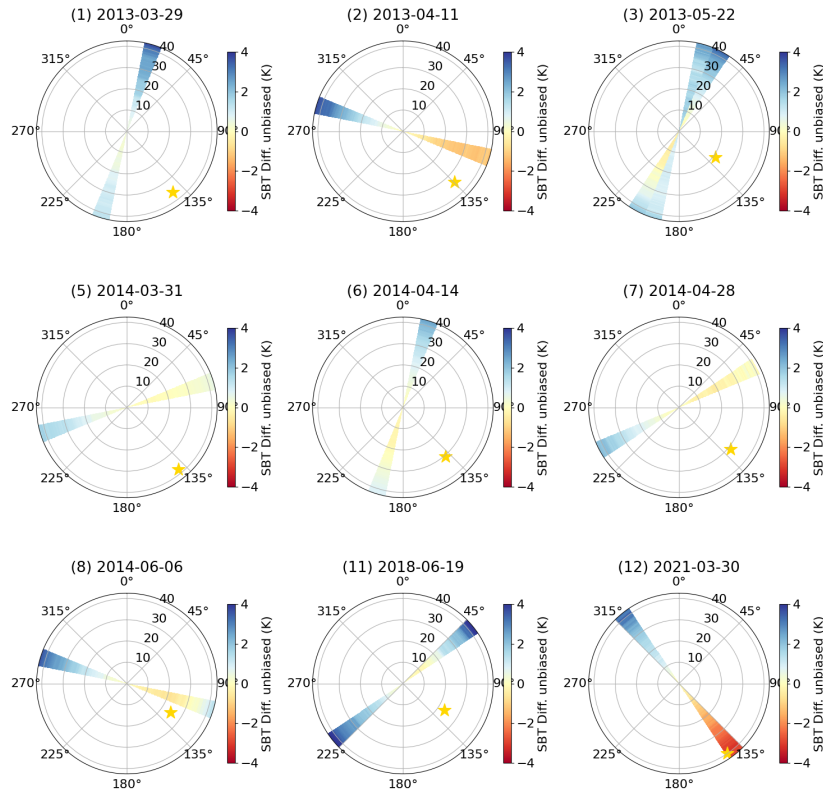


Figure 6: SBT difference (Landsat-8 - MASTER) with respect to MASTER view zenith and azimuth, corrected of the bias computed in table 6. Average sun position is marked by an orange star. (negative values are in red and mean that MASTER is warmer than Landsat-8)

358 Figure 7 allows better observing those two configurations. It shows the distribu-
 359 tions of the bias-corrected SBT with respect to MASTER signed VZA (positive angle
 360 are to the east and therefore closer to the sun, negative to the west). The dotted red line
 361 indicates the mean difference, while the dashed red lines indicate ± 1 standard devia-
 362 tion. In configurations (2), (8) and (12) where the sun is almost in the principal plane
 363 and close to hotspot, MASTER SBT gets steadily warmer than Landsat-8 from east to
 364 west. For track (8), SBT starts to get colder past the sun zenith. For tracks (1), (3),
 365 (5), (6), (7) and (11), MASTER gets colder on both end of the swath, with a varying

366 position for the maximum position, which may be related to gap fraction. Dotted blue
 367 vertical lines indicate the FOV of the up-comping TRISHNA and SBG missions. One
 368 can note that the 1 standard deviation red dashed lines show that the standard deviation
 369 is almost constant throughout the MASTER signed VZA, and equal to standard
 370 deviation estimated in table 6. This standard deviation therefore probably accounts for
 371 uncertainties between sensors that are not related to TIR anisotropy.

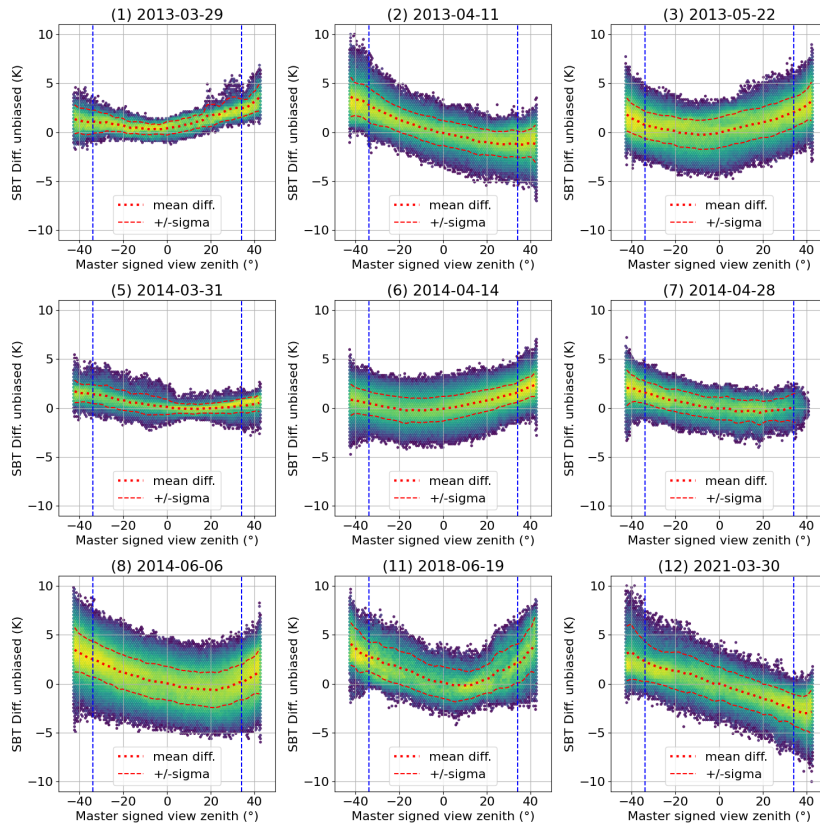


Figure 7: SBT difference, corrected of the bias computed in table 6, with respect to MASTER signed view zenith angle (positive angles are to the east, negative to the west). The solid red line indicates the mean values, the red dashed line indicates mean \pm 1 standard deviation. Blue dotted lines indicate TRISHNA and SBG FOV.

372 Table 7 gives a quantitative analysis of the directional effects budget for each track,
 373 based on the mean difference trend for each track (see dotted red curves in figure 7).

374 Within MASTER FOV, the amplitude of directional effects ranges from 1.5K to more
 375 than 6K for track (12), the closest track to hotspot conditions. Restricted to the foreseen
 376 TRISHNA and SBG FOV, this budget value falls to 4.7K.

id	MASTER				Trishna			
	Min.	-43°	43°	amp.	Min.	-34°	34°	amp.
(1) 2013-03-29	0.3	1.3	3.6	3.3	0.3	1.1	2.5	2.2
(2) 2013-04-11	-1.3	3.6	-1.2	4.9	-1.2	2.6	-1.2	3.9
(3) 2013-05-22	-0.3	1.8	3.2	3.4	-0.3	0.7	1.9	2.2
(5) 2014-03-31	-0.1	1.7	0.5	1.8	-0.1	1.4	0.2	1.5
(6) 2014-04-14	-0.3	0.8	2.4	2.7	-0.3	0.4	1.5	1.7
(7) 2014-04-28	-0.5	2.0	0.1	2.5	-0.5	1.5	-0.0	2.0
(8) 2014-06-06	-0.7	3.5	1.2	4.1	-0.7	2.5	0.1	3.1
(11) 2018-06-19	-0.2	4.1	4.0	4.3	-0.2	2.7	2.0	2.9
(12) 2021-03-30	-3.0	3.1	-2.9	6.3	-2.4	2.2	-2.5	4.7

Table 7: For each MASTER track, minimum average SBT difference, average SBT difference at both ends of swath and amplitude (amp.) of SBT difference between minimum and maximum are displayed, left for the MASTER FOV, right, for a limitation to TRISHNA FOV (all in K). The max-min column gives an estimate of directional effects.

377 3.2.3. Sensitivity to land-cover

378 Figure 8 shows the mean and standard deviation curves of SBT difference with re-
 379 spect to MASTER signed view zenith angle, for the major land-cover classes (> 15%)
 380 highlighted in table 5. It can be observed that though slight differences may appear
 381 between classes on the same track, most of the time all classes follow a similar trend
 382 for a given track. The NDVI strata seems to be the main driver for consistency, as can
 383 be noted on track (1) and (5) with bare soil and low vegetation with low NDVI, on
 384 track (3) with forests and low vegetation, both with intermediate NDVI, and on track
 385 (8) between croplands and low vegetation, both with a low NDVI. On track (6), it can
 386 be observed that the urban class behaves very similarly to the low vegetation with low
 387 NDVI class, which may indicate that urban class is actually a fair mix of artificial and

388 vegetated surfaces. Track (3) might exhibit some sort of gap fraction effect, with in-
389 termediate NDVI classes getting to a lower minimum than low NDVI classes. Forests
390 with high NDVI seem to behave slightly differently than other intermediate NDVI veg-
391 etation classes, with only two examples on track (7) and (12). Interestingly, forests
392 with high NDVI also exhibit a smaller standard deviation with respect to other classes.
393 Some kind of ordering can be observed for instance on track (7) and (11), with lower
394 NDVI classes yielding lower differences.

395 It should however be noted that in most of the cases, mean curves of each classes are
396 within the \pm standard-deviation of other classes. This seems to indicate that in the 100
397 meter resolution range, with this combination of limited dataset and land-cover source,
398 pixels are mixed and exhibit average directional trends rather than sharp vegetation
399 or crop types related signatures. Due to the severe classes imbalance between tracks,
400 estimating model parameters independently on each class would further reduce the
401 variability of angular configurations and thus the significance of the experiment. A
402 much larger dataset would be necessary for per-class estimation of models parameters.
403 In the next section, model estimations will therefore only be performed jointly for all
404 classes.

405 *3.3. Directional model fitting*

406 *3.3.1. Per-track parameters estimation*

407 In this section, each of the five models presented in table 3 is fitted independently
408 on de-biased SBT from each track, using the methodology presented in 2.3. Models are
409 fitted using all pixels from all land-cover classes of a track, which provides the required
410 variability to fit the 3 to 4 parameters depending on the model. Figure 9 shows how
411 each model fits the scatter plot for each track. SBT differences are expressed as a
412 percentage variation to facilitate the comparison with the model. All models seem to
413 be able to fit the observed directional effects, with the RL and LSF-RL being slightly
414 more versatile than the other, and the Vinnikov model struggling to cope with higher
415 VZA. This can be observed for instance on tracks (2) and (12) where the Vinnikov
416 model diverges below 0° . Hotspot shape seems to be correctly captured by the other
417 four models in track (2), (8) and (12). Differences for all models start to show for

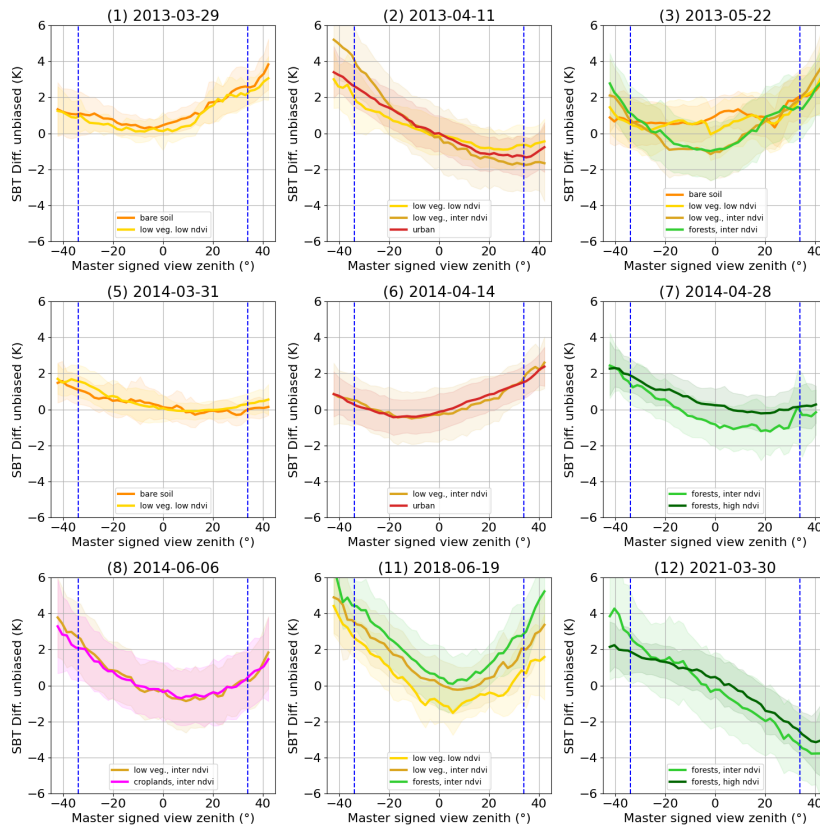


Figure 8: Mean \pm standard-deviation of unbiased SBT difference with respect to MASTER signed view zenith angle for the major land-cover classes (> 15%) of each land cover classes as highlighted in table 5.

418 higher viewing angles close to or outside limits of the data range.

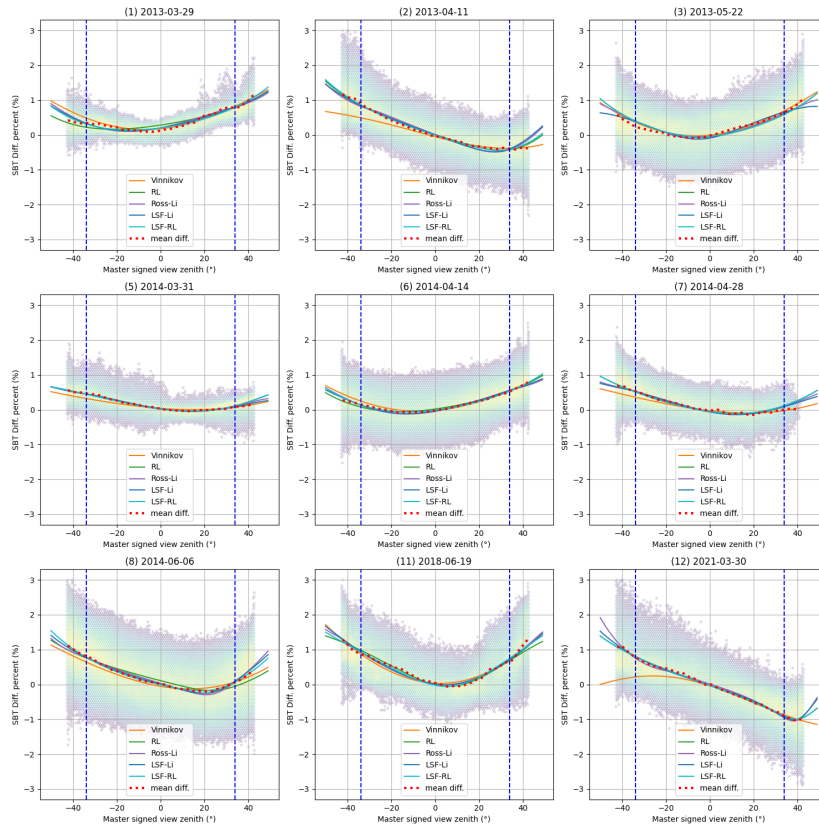


Figure 9: Least-Square fitting of the five TIR directional models from table 3 on SBT differences. Vertical axis represent the percentage of variation of SBT between Landsat-8 (considered as Nadir) and MASTER. In this figure, each model is fitted separately on each track.

419 In table 8, the correction performance of each model is measured for each track in
 420 terms of Root Mean Squared Error (RMSE) and amplitude (max - min of red curve
 421 in figure 7). Regarding RMSE, it can be observed that all models allow reducing the
 422 RMSE with respect to the uncorrected values. Though performances on RMSE im-
 423 provement are very close from one model to another, the LSF-Li reaches the best per-
 424 formances for 8 tracks out of 9, while the Ross-Li and LSF-RL models reaches the best
 425 performances on 7 tracks out of 9. On track (12), which is the closest to the hotspot,
 426 all models seem to perform almost equally. Gains on RMSE range from 0.2K to 0.9K

427 depending on the track.

428 In [Cao et al. \(2019\)](#), lower RMSE are found on simulated data (bellow 0.5K). Thea
 429 authors recommend the following ranking for models (best to worst) : LSF-Li, Ross-
 430 Li, Vinnikov and RL. This is consistent with RMSE on table 8 with the LSF-Li being
 431 the best model 8 times out of 9, the Ross-Li, Vinnikov and LSF-RL models 7 times out
 432 of 9, and the RL model only 5 times out of 9.

433 In terms of directional effects amplitude, table 8 shows that all models allow to
 434 significantly reduce the amplitude, below 1 K for the majority of tracks. Reductions
 435 for tracks with high hotspot effects are particularly strong, with track (12) going from
 436 more than 6K to less than 0.7 K for instance. The Vinnikov model is the best model
 437 for more than half of the tracks, but tracks with strong hotspot effect such as (8) and
 438 (12) are won by either RL, LSF-Li or LSF-RL. Regarding amplitude, performances
 439 of the different models are less close to each others, but this can be explained by the
 440 use of maximum - minimum difference, which is highly sensitive to outliers. Gains on
 441 directional effects amplitude range from 1.6K to 5.8K depending on the track.

id	RMSE						Amp					
	Raw	Vin.	RL	Ross	LSF	LRL	Raw	Vin.	RL	Ross	LSF	LRL
(1)	1.8	1.0	1.0	1.0	1.0	1.0	3.3	0.6	1.4	1.0	0.8	0.9
(2)	2.3	1.5	1.5	1.5	1.5	1.5	4.9	0.3	0.6	1.1	1.1	0.7
(3)	2.0	1.5	1.6	1.6	1.5	1.6	3.4	0.5	1.2	1.0	1.2	0.9
(5)	1.1	0.8	0.8	0.8	0.8	0.8	1.8	0.4	0.4	0.3	0.2	0.4
(6)	1.6	1.2	1.2	1.2	1.2	1.2	2.7	0.2	0.4	0.6	0.5	0.3
(7)	1.6	1.2	1.2	1.2	1.2	1.2	2.5	0.3	0.9	0.8	0.8	0.9
(8)	2.3	1.8	1.9	1.8	1.8	1.8	4.1	0.8	1.3	0.7	0.4	0.2
(11)	2.8	1.9	1.9	1.9	1.9	1.8	4.3	1.1	1.4	0.9	1.0	1.0
(12)	2.7	1.9	1.9	1.8	1.8	1.9	6.3	0.7	0.5	0.7	0.5	0.5

Table 8: Root Mean-Square error and amplitude (max - min of red curve in figure 7) for raw SBT corrected of the bias computed in table 6, and for MASTER temperature normalized with five models, with parameters estimated for each track. Note that model names have been shortened (Vin: Vinnikov, RL: Roujean-Lagouarde, Ross: Ross-Li, LSF: LSF-Li, LRL: LSF-RL).

442 Figure 10 shows the raw and corrected SBT with respect to the signed VZA for 5
443 tracks with very strong directional effects. It can be noted that the correction does not
444 seem to have any effect on the standard-deviation, and thus it does not amplify or create
445 any noise. For track (2), the best model in terms of amplitude is Vinnikov according
446 to table 8, closely followed by RL and LSF, though it can be observed that the Ross-Li
447 and LSF-Li models struggle at higher VZA (out of TRISHNA FOV). For track (3), the
448 best model is also Vinnikov, with amplitude two times less than the next best model,
449 which is RL. Indeed, the latter seems to fail to completely compensate the directional
450 trends, with SBT differences still slightly positives for positive VZA and negative for
451 negative VZA. On track (8), the best model is LSF-RL by a large amount according to
452 table 8, which is confirmed on figure 10 with a smooth a regular corrected SBT.

453 Although directional trends are considerably reduced after correction, there are re-
454 maining trends in almost all models, and all of them struggle at higher VZA. Track (11)
455 is noisier and the model fitting is poorer, with only the Ross-Li model achieving a cor-
456 rection with an amplitude below 1 K, though differences on figure 10 are not obvious.
457 For track (12), which is the track with the strongest hotspot effect due to the proxim-
458 ity of MASTER viewing direction and solar direction (see figure 6), LSF-Li, RL and
459 LSF-RL models have the best performances according to table 8 which is confirmed
460 on figure 10 by fewer oscillations for higher VZA.

461 3.3.2. *Global models parameters estimation*

462 Fitting models on each track separately allows to assess how well those models ex-
463 plain the observed data. However, this strategy does not apply to operational directional
464 corrections in ground segments, where simultaneous observations will not be available
465 to fit the models. This section investigates the performances of global models, with
466 a single set of parameters for each model to correct all tracks at once. Parameters of
467 those global models are fitted on all pixels from all tracks altogether, using the method-
468 ology presented in 2.3. Figure 11 shows how well those global models fit the scatter
469 plots for each track. It can be observed that even if the goodness of fit is lesser than in
470 figure 9, it is still relatively high. However, global models also struggle to model the
471 near hotspot conditions of track (12).

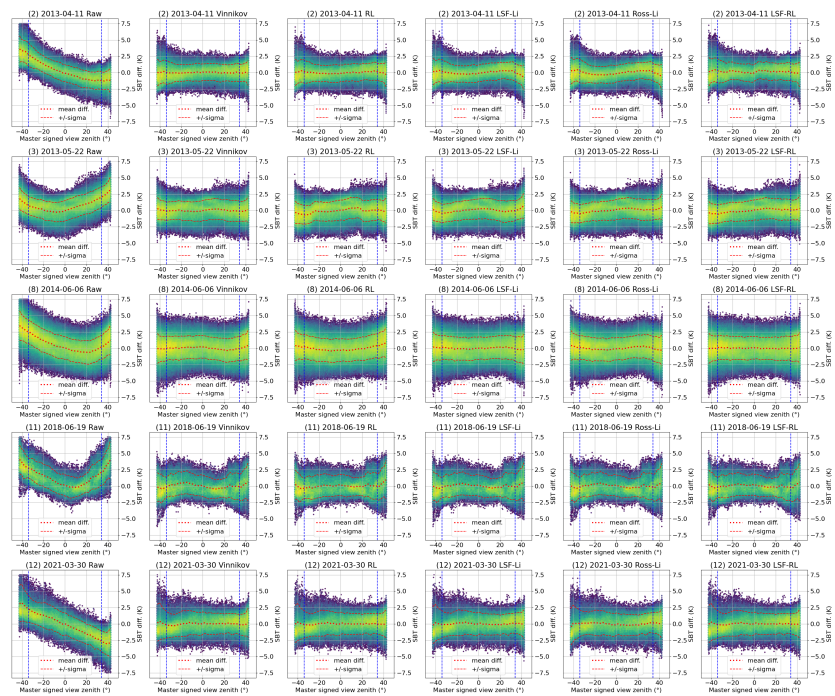


Figure 10: Corrected SBT versus signed VZA for raw and model-corrected SBT, for 5 tracks with high directional effects amplitudes. Blue dashed lines indicate Trishna FOV.

472 Table 9 shows the quantitative performance analysis of global models. As in table
473 8, no model clearly outperform the others. All models achieve a systematic decrease
474 of RMSE ranging from 0.2K to 0.9K and a systematic decrease of directional effects
475 amplitude ranging from 1.3K to 4.8K. Even if their performances are lower than those
476 achieved by per track models presented in section 3.3.1, global models still provide
477 valuable corrections. It can be observed that if the RL model is frequently the best
478 model in terms of RMSE, it is never the best model in terms of amplitude. The ranking
479 according to the number of times a model is the best model in terms of RMSE is the
480 following (best to worst) : RL, LSF-RL, Vinnikov and LSF-Li, Ross-Li. This ranking
481 differs from the ranking of Cao et al. (2019), in which models are not fitted globally.

id	RMSE						Amp					
	Raw	Vin.	RL	Ross	LSF	LRL	Raw	Vin.	RL	Ross	LSF	LRL
(1)	1.8	1.2	1.3	1.0	1.0	1.2	3.3	1.2	1.2	1.6	0.9	1.0
(2)	2.3	1.5	1.6	1.6	1.6	1.6	4.9	1.0	1.8	1.8	2.2	2.0
(3)	2.0	1.6	1.6	1.6	1.6	1.6	3.4	1.2	1.3	1.4	1.2	1.4
(5)	1.1	0.9	0.8	1.2	1.1	0.8	1.8	1.1	0.6	0.5	1.1	0.7
(6)	1.6	1.2	1.2	1.2	1.2	1.2	2.7	0.6	0.5	0.7	0.7	0.3
(7)	1.6	1.2	1.2	1.3	1.3	1.2	2.5	0.8	0.9	1.0	1.4	1.0
(8)	2.3	1.9	1.9	2.0	1.9	1.9	4.1	1.4	1.9	1.9	1.0	1.4
(11)	2.8	2.2	1.9	2.2	2.1	1.9	4.3	2.8	2.1	2.8	1.9	1.9
(12)	2.7	2.1	2.0	2.1	2.0	2.1	6.3	2.5	2.7	1.7	1.5	3.2

Table 9: Root Mean-Square error and amplitude (max - min of red curve in figure 7) for raw SBT corrected of the bias computed in table 6, and for MASTER temperature normalized with five models, with parameters jointly estimated on all tracks. Note that model names have been shortened (Vin: Vinnikov, RL: Roujean-Lagouarde, Ross: Ross-Li, LSF: LSF-Li, LRL: LSF-RL).

482 Figure 12 presents the same tracks as in figure 10 but corrected with the global
483 models. While all tracks exhibit residual angular trends, within the TRISHNA FOV,
484 all models exhibit performances that may be of interest for downstream applications.
485 Track (11) has the highest residual effects, which is compliant with figures in table 9,

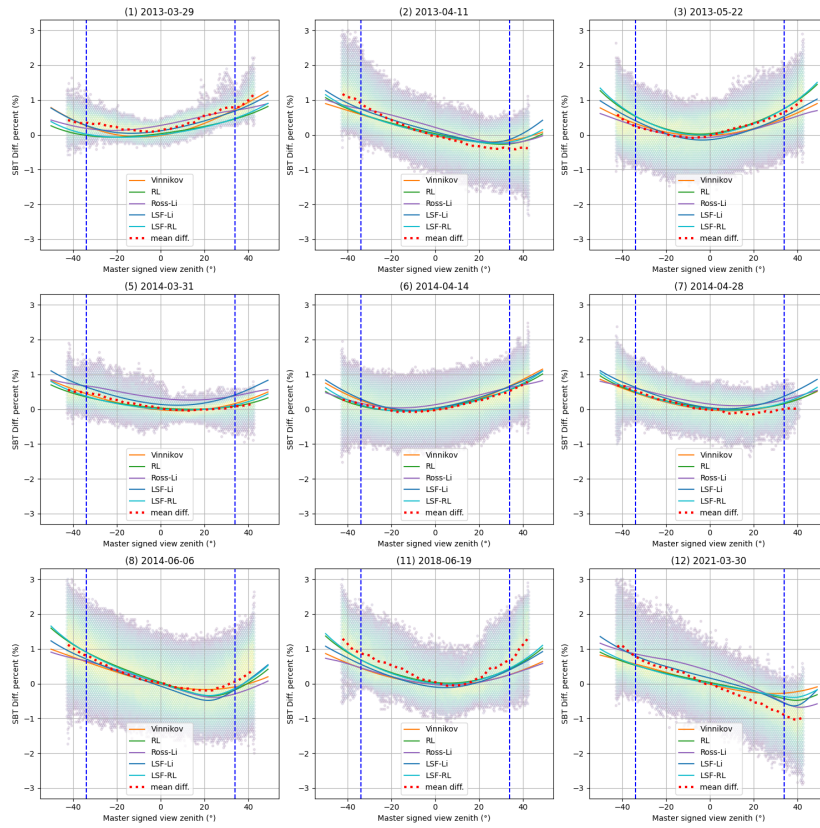


Figure 11: Least-Square fitting of the five TIR directional models from table 3 on SBT differences. Vertical axis represent the percentage of variation of SBT between Landsat-8 (considered as Nadir) and MASTER. In this figure, each model is jointly fitted on all tracks.

486 showing a residual amplitude of around 2K for all models. On track (12), which is the
 487 closest to hotspot conditions, the Vinnikov and LSF-RL model perform poorly with
 488 respect to the other models, the former even introduces an artificial angular trend while
 489 the latter fails to completely capture the angular tend. All remaining models on track
 490 (12) significantly reduce the angular trend that can be observed in raw SBT differences.

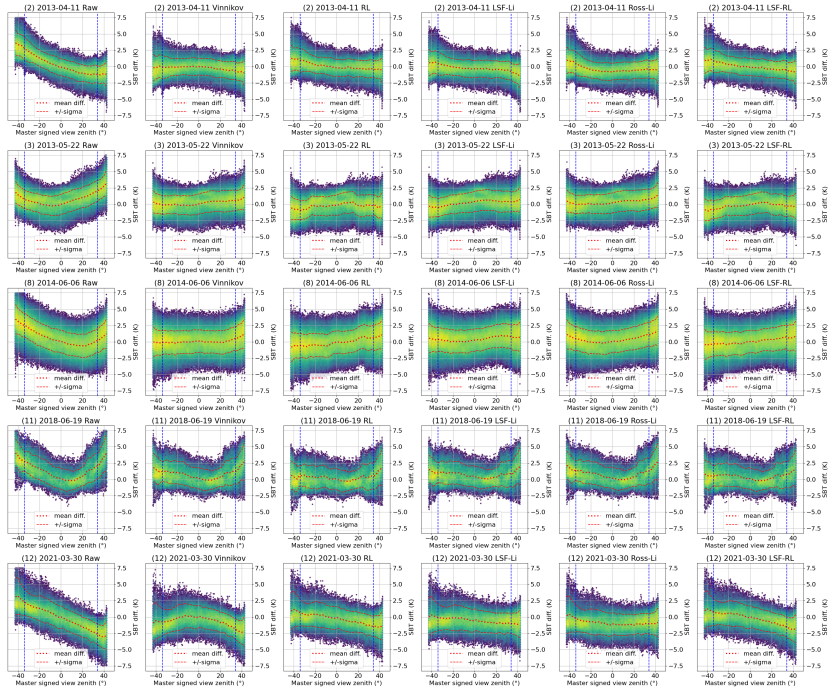


Figure 12: Corrected SBT versus signed VZA for raw and model-corrected SBT, using models jointly fitted on all tracks, for 5 tracks with high directional effects amplitudes. Blue dashed lines indicate TRISHNAP FOV.

491 Figure 13 presents a complete viewing angles sampling of each global model, in
 492 the mean solar conditions of track (12). All models seem to have captured the hotspot
 493 effect, while the shape of the hotspot itself varies from one model to another. the
 494 Vinnikov model hotspot seems ahead of the sun zenith angle, which may explain its
 495 lesser performance in correcting track (12). Table 10 shows the estimated parameters
 496 for each model. One can note that the Ross-Li Volumetric kernel contribution is very
 497 low with respect to the others.

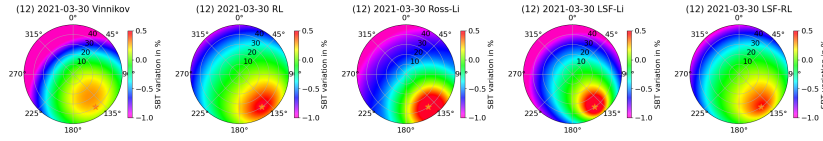


Figure 13: Polar plot of the different models, jointly fitted on all tracks, using average solar angles of track (12). Sun position is indicated by an orange star mark.

Model	k_0	k_1	k_2	k_{hs}
Ross-Li	1	-7.4e-16	0.0091	
LSF-Li	1.2	-0.22	0.011	
Vinnikov	1	-0.023	0.024	
RL	1		0.0061	1.8e-07
LSF-RL	1	-0.047	0.0058	9.7e-07

Table 10: Parameters of the global models, estimated from all pairs

498 4. Discussion

499 This study exhibits evidences of strong directional effects up to an amplitude of
500 6K within a FOV of $\pm 45^\circ$, with real high-resolution TIR data, and shows encouraging
501 performances of state-of-the art parametric models to mitigate their impact on temper-
502 ature accuracy. However, two aspects of this work need to be further analysed and
503 discussed: the inherent limitations related to the scarce data availability on one hand,
504 and the derivation of the model parameters in a real-world ground segment scenario.

505 4.1. Limitations of the study

506 Due to the scarce availability of simultaneous observations between MASTER and
507 Landsat-8 on one hand, and the limited coverage of MASTER flights on the other, this
508 study only covers a limited range of landscapes, all of them located in California, USA.
509 Therefore, it can not be used to draw solid conclusions on other kinds of landscapes
510 such as desert bare soil, very dense rain-forest canopy or tundras for instance. The ge-
511 ographic limitations also come with a low variety of solar angle conditions, excluding
512 extreme latitudes and equator for instance.

513 Moreover, since this study relies on Landsat-8 acquisitions which have a local over-
514 passing time of approximately 10:30 AM, its results are mainly valid for medium morn-
515 ing sun angles, whereas most upcoming missions will have a local over-passing time
516 around noon. The solar zenith angle will therefore be lower, leading to solar angular
517 conditions that have not been analysed in this study. As hotspot conditions will be
518 more frequent, It is conjectured to observe lower but more frequent directional effects
519 for sun position closer to zenith, but in the mean time SBT values could be higher.

520 Finally, this study adopts an indiscriminating point of view regarding the actual
521 land-cover of each pixel, whereas the literature, which is driven by work on radiative
522 transfer modeling, strongly suggests that different models or at least model parameters
523 should be applied to different land-covers. We analysed the influence of land-cover on
524 TIR anisotropy in section 3.2.3. We observed that classes seem to be mixed in our 100
525 meter resolution dataset, and exhibit similar angular trends. The land-cover agnostic
526 approach was therefore privileged. However, this could be revisited if a larger dataset
527 was to be acquired, with more landscape variability. It must be stressed that if a direc-
528 tional effect correction is to be implemented into up-coming missions ground-segment
529 as a routine level 2 processing, relying on land-cover discrimination and phenology
530 will be hard to achieve for a global coverage mission. Nevertheless, exogenous land-
531 cover and phenology maps could be used for that purpose (Phiri et al., 2020). Last,
532 TIR directional effects in urban environment follow very different physical causes and
533 trends (Lagouarde and Irvine, 2008; Lagouarde et al., 2010), and may require different
534 models, such as the combinations of base kernels investigated in Jiang et al. (2021).

535 4.2. Model parameters estimation for up-coming ground segments

536 Another open question is whether such a correction is to be implemented within
537 future ground segments and which credit to give to the estimated model parameters
538 over time. In this study, models have first been fitted to each track independently, re-
539 sulting in good correction performances of up to 5.8K in amplitude, but with important
540 variations of the parameters from one track to another. Such variability suggests that
541 model parameters might depend on the canopy structure as well as on the observation
542 conditions they are fitted to. For instance, the RL kernel, is the best performing kernel

543 for track (12) that is closest to hotspot condition, which can be explained either because
544 this model is a good model for hotspot or because it requires hotspot condition to be
545 fitted properly. It must however again be stressed that such scene based individual pa-
546 rameters estimation is out of reach for routinely correcting data from global coverage
547 satellites such as TRISHNA, LSTM or SBG.

548 On the other hand, the global models that have been fitted simultaneously on all
549 tracks still exhibit interesting correction performances of up to 4.7K in the studied
550 tracks. This work therefore suggests that such global models could be used routinely
551 in a ground segment and be beneficial for downstream applications, with the limitations
552 already highlighted in section 4.1.

553 While the determination of factors that should drive model parameters is probably
554 best served by the physical process modelling scientific community, this paper pro-
555 poses valuable dataset and methodology to assess model performances before putting
556 them into production. Though in this work the analysed data are limited to 9 tracks
557 in California, in the future, MASTER or other airborne TIR sensors with wide FOVs
558 might be used to acquire more of those simultaneous observations with the Landsat
559 series, effectively building a database for the assessment and calibration of directional
560 parametric models, should attention be paid to the simultaneous over-passing time.

561 **5. Conclusion**

562 In this paper, simultaneous observations in space and time between Landsat-8 and
563 the wide FOV MASTER airborne TIR sensors have been leveraged to analyse potential
564 directional effects and their error budget for up-coming High Resolution TIR missions.
565 Nine MASTER tracks were identified with a Landsat-8 overpass during the flight and
566 the analysis of their SBT differences exhibits directional effects ranging from 1.6K to
567 more than 6K within MASTER full FOV depending to the proximity to hotspot con-
568 ditions. Three tracks are close to those conditions and one is almost within the prin-
569 cipal acquisition plane, leading to the highest 6K amplitude. Other tracks also exhibit
570 evidences of the gap fraction effect. Five state-of-the-art parametric models for TIR
571 anisotropy have been selected from the literature for having been extensively tested on

572 simulated data. Those five models have been fitted to each of the identified MASTER
573 track, using Landsat-8 as the target Nadir SBT of reference. The corrected temperature
574 exhibits a systematic decrease of the RMSE of 0.2K to 0.9K, and a reduction of the am-
575 plitude associated to directional effects of 1.6K to 5.8K, bringing down the directional
576 error budget to less than 1K in almost all cases. Global models, fitted simultaneously on
577 all valid tracks, have also been assessed, with a reduction of RMSE of 0.2K to 0.8K and
578 a reduction of the directional effect amplitude of 1.3K to 4.7K, bringing down the di-
579 rectional error budget below 2K in most cases. Those results suggest that future ground
580 segments of up-coming high-resolution missions with a FOV greater than 30° would
581 benefit from implementing such a correction. While in theory the LSF-RL model is the
582 most suited to account for both the gap fraction and hotspot effects observed in figure
583 6, the LSF-RL model does not significantly outperform the other models in this study,
584 which may be due to the limited amount of data, especially for the fitting of its extra
585 parameter. This paper also lays grounds for a directional model in flight calibration
586 procedure for those up-coming missions, should more airborne data be gathered during
587 Landsat overpasses in the future.

588 The data used in this study have been made publicly available as an open dataset (Michel
589 et al., 2023).

590 References

- 591 M. Anderson, J. Norman, W. Kustas, R. Houborg, P. Starks, N. Agam, A
592 thermal-based remote sensing technique for routine mapping of land-surface car-
593 bon, water and energy fluxes from field to regional scales, *Remote Sensing*
594 of Environment 112 (2008) 4227–4241. URL: <https://www.sciencedirect.com/science/article/pii/S0034425708002289>. doi:<https://doi.org/10.1016/j.rse.2008.07.009>.
- 597 J. C. Price, Estimation of Regional Scale Evapotranspiration Through Analysis of
598 Satellite Thermal-infrared Data, *IEEE Transactions on Geoscience and Remote*
599 *Sensing* GE-20 (1982) 286–292. doi:[10.1109/TGRS.1982.350445](https://doi.org/10.1109/TGRS.1982.350445), conference
600 Name: IEEE Transactions on Geoscience and Remote Sensing.

- 601 D. Courault, B. Seguin, A. Olioso, Review on estimation of evapotranspiration from
602 remote sensing data: From empirical to numerical modeling approaches, *Irrigation
603 and Drainage Systems* 19 (2005) 223–249. URL: [https://doi.org/10.1007/
604 s10795-005-5186-0](https://doi.org/10.1007/s10795-005-5186-0). doi:10.1007/s10795-005-5186-0.
- 605 M. C. Anderson, R. G. Allen, A. Morse, W. P. Kustas, Use of Landsat thermal im-
606 agery in monitoring evapotranspiration and managing water resources, *Remote
607 Sensing of Environment* 122 (2012) 50–65. URL: [https://www.sciencedirect.
608 com/science/article/pii/S0034425712000326](https://www.sciencedirect.com/science/article/pii/S0034425712000326). doi:10.1016/j.rse.2011.
609 08.025.
- 610 G. Boulet, B. Mougenot, J.-P. Lhomme, P. Fanise, Z. Lili-Chabaane, A. Olioso,
611 M. Bahir, V. Rivalland, L. Jarlan, O. Merlin, B. Coudert, S. Er-Raki, J.-
612 P. Lagouarde, The SPARSE model for the prediction of water stress and
613 evapotranspiration components from thermal infra-red data and its evaluation
614 over irrigated and rainfed wheat, *Hydrology and Earth System Sciences*
615 19 (2015) 4653–4672. URL: [https://hess.copernicus.org/articles/19/
616 4653/2015/](https://hess.copernicus.org/articles/19/4653/2015/). doi:10.5194/hess-19-4653-2015, publisher: Copernicus GmbH.
- 617 R. Ishimwe, K. Abutaleb, F. Ahmed, et al., Applications of thermal imaging in agri-
618 culture—a review, *Advances in remote Sensing* 3 (2014) 128.
- 619 J.-P. Lagouarde, B. Bhattacharya, P. Crébassol, P. Gamet, S. S. Babu, G. Boulet,
620 X. Briottet, K. Buddhiraju, S. Cherchali, I. Dadou, G. Dedieu, M. Gouhier,
621 O. Hagolle, M. Irvine, F. Jacob, A. Kumar, K. K. Kumar, B. Laignel, K. Mallick,
622 C. Murthy, A. Olioso, C. Ottlé, M. R. Pandya, P. V. Raju, J.-L. Roujean, M. Sekhar,
623 M. V. Shukla, S. K. Singh, J. Sobrino, R. Ramakrishnan, The Indian-French Trishna
624 Mission: Earth Observation in the Thermal Infrared with High Spatio-Temporal
625 Resolution, in: *IGARSS 2018 - 2018 IEEE International Geoscience and Remote
626 Sensing Symposium, 2018*, pp. 4078–4081. doi:10.1109/IGARSS.2018.8518720,
627 iSSN: 2153-7003.
- 628 K. Cawse-Nicholson, P. A. Townsend, D. Schimel, A. M. Assiri, P. L. Blake, M. F.
629 Buongiorno, P. Campbell, N. Carmon, K. A. Casey, R. E. Correa-Pabón, K. M.

630 Dahlin, H. Dashti, P. E. Dennison, H. Dierssen, A. Erickson, J. B. Fisher, R. Frouin,
631 C. K. Gatebe, H. Gholizadeh, M. Gierach, N. F. Glenn, J. A. Goodman, D. M. Grif-
632 fith, L. Guild, C. R. Hakkenberg, E. J. Hochberg, T. R. H. Holmes, C. Hu, G. Hul-
633 ley, K. F. Huemmrich, R. M. Kudela, R. F. Kokaly, C. M. Lee, R. Martin, C. E.
634 Miller, W. J. Moses, F. E. Muller-Karger, J. D. Ortiz, D. B. Otis, N. Pahlevan, T. H.
635 Painter, R. Pavlick, B. Poulter, Y. Qi, V. J. Realmuto, D. Roberts, M. E. Schaepman,
636 F. D. Schneider, F. M. Schwandner, S. P. Serbin, A. N. Shiklomanov, E. N. Stavros,
637 D. R. Thompson, J. L. Torres-Perez, K. R. Turpie, M. Tzortziou, S. Ustin, Q. Yu,
638 Y. Yusup, Q. Zhang, NASA's surface biology and geology designated observable:
639 A perspective on surface imaging algorithms, *Remote Sensing of Environment* 257
640 (2021) 112349. URL: [https://www.sciencedirect.com/science/article/
641 pii/S0034425721000675](https://www.sciencedirect.com/science/article/pii/S0034425721000675). doi:10.1016/j.rse.2021.112349.

642 B. Koetz, W. Bastiaanssen, M. Berger, P. Defournay, U. Del Bello, M. Drusch,
643 M. Drinkwater, R. Duca, V. Fernandez, D. Ghent, R. Guzinski, J. Hoogeveen,
644 S. Hook, J.-P. Lagouarde, G. Lemoine, I. Manolis, P. Martimort, J. Masek, M. Mas-
645 sart, C. Notarnicola, J. Sobrino, T. Udelhoven, High Spatio- Temporal Resolution
646 Land Surface Temperature Mission - a Copernicus Candidate Mission in Support of
647 Agricultural Monitoring, in: *IGARSS 2018 - 2018 IEEE International Geoscience
648 and Remote Sensing Symposium*, 2018, pp. 8160–8162. doi:10.1109/IGARSS.
649 2018.8517433, iSSN: 2153-7003.

650 S. Mwangi, G. Boulet, A. Olioso, Assessment of an extended sparse model for esti-
651 mating evapotranspiration from directional thermal infrared data, *Agricultural and
652 Forest Meteorology* 317 (2022) 108882. URL: [http://dx.doi.org/10.1016/j.
653 agrformet.2022.108882](http://dx.doi.org/10.1016/j.agrformet.2022.108882). doi:10.1016/j.agrformet.2022.108882.

654 Z.-L. Li, B.-H. Tang, H. Wu, H. Ren, G. Yan, Z. Wan, I. F. Trigo, J. A. Sobrino,
655 Satellite-derived land surface temperature: Current status and perspectives, *Remote
656 Sensing of Environment* 131 (2013) 14–37. URL: [http://dx.doi.org/10.1016/
657 j.rse.2012.12.008](http://dx.doi.org/10.1016/j.rse.2012.12.008). doi:10.1016/j.rse.2012.12.008.

- 658 D. L. Jupp, A. H. Strahler, A hotspot model for leaf canopies, *Remote Sensing of*
659 *Environment* 38 (1991) 193–210.
- 660 T. Nilson, Inversion of gap frequency data in forest stands, *Agricultural and For-*
661 *est Meteorology* 98-99 (1999) 437–448. URL: [http://dx.doi.org/10.1016/](http://dx.doi.org/10.1016/S0168-1923(99)00114-8)
662 [S0168-1923\(99\)00114-8](http://dx.doi.org/10.1016/S0168-1923(99)00114-8). doi:10.1016/s0168-1923(99)00114-8.
- 663 B. Cao, J.-L. Roujean, J.-P. Gastellu-Etchegorry, Q. Liu, Y. Du, J.-P. Lagouarde,
664 H. Huang, H. Li, Z. Bian, T. Hu, B. Qin, X. Ran, Q. Xiao, A general framework
665 of kernel-driven modeling in the thermal infrared domain, *Remote Sensing of Envi-*
666 *ronment* 252 (2021) 112157. URL: [http://dx.doi.org/10.1016/j.rse.2020.](http://dx.doi.org/10.1016/j.rse.2020.112157)
667 [112157](http://dx.doi.org/10.1016/j.rse.2020.112157). doi:10.1016/j.rse.2020.112157.
- 668 J.-P. Lagouarde, S. Dayau, P. Moreau, D. Guyon, Directional anisotropy of brightness
669 surface temperature over vineyards: Case study over the medoc region (sw france),
670 *IEEE Geoscience and Remote Sensing Letters* 11 (2014) 574–578. doi:10.1109/
671 [LGRS.2013.2282492](https://doi.org/10.1109/LGRS.2013.2282492).
- 672 J. A. Sobrino, J. Cuenca, Angular variation of thermal infrared emissivity for some
673 natural surfaces from experimental measurements, *Applied Optics* 38 (1999)
674 3931. URL: <http://dx.doi.org/10.1364/ao.38.003931>. doi:10.1364/ao.
675 [38.003931](https://doi.org/10.1364/ao.38.003931).
- 676 S. L. Ermida, I. F. Trigo, G. Hulley, C. C. DaCamara, A multi-sensor approach to re-
677 trieve emissivity angular dependence over desert regions, *Remote Sensing of Envi-*
678 *ronment* 237 (2020) 111559. URL: [http://dx.doi.org/10.1016/j.rse.2019.](http://dx.doi.org/10.1016/j.rse.2019.111559)
679 [111559](http://dx.doi.org/10.1016/j.rse.2019.111559). doi:10.1016/j.rse.2019.111559.
- 680 J.-L. Roujean, M. Leroy, P.-Y. Deschamps, A bidirectional reflectance model of the
681 earth's surface for the correction of remote sensing data, *Journal of Geophys-*
682 *ical Research* 97 (1992) 20455. URL: <http://dx.doi.org/10.1029/92jd01411>.
683 doi:10.1029/92jd01411.
- 684 W. Wanner, X. Li, A. H. Strahler, On the derivation of kernels for kernel-driven models

- 685 of bidirectional reflectance, *Journal of Geophysical Research* 100 (1995) 21077.
686 URL: <http://dx.doi.org/10.1029/95jd02371>. doi:10.1029/95jd02371.
- 687 J.-L. Roujean, A parametric hot spot model for optical remote sensing applications,
688 *Remote Sensing of Environment* 71 (2000) 197–206. URL: [http://dx.doi.org/](http://dx.doi.org/10.1016/s0034-4257(99)00080-2)
689 [10.1016/s0034-4257\(99\)00080-2](http://dx.doi.org/10.1016/s0034-4257(99)00080-2). doi:10.1016/s0034-4257(99)00080-2.
- 690 M. Claverie, J. Ju, J. G. Masek, J. L. Dungan, E. F. Vermote, J.-C. Roger, S. V.
691 Skakun, C. Justice, The harmonized landsat and sentinel-2 surface reflectance
692 data set, *Remote Sensing of Environment* 219 (2018) 145 – 161. doi:<https://doi.org/10.1016/j.rse.2018.09.002>.
693 [//doi.org/10.1016/j.rse.2018.09.002](https://doi.org/10.1016/j.rse.2018.09.002).
- 694 C. Duffour, J.-P. Lagouarde, A. Olioso, J. Demarty, J.-L. Roujean, Driving factors of
695 the directional variability of thermal infrared signal in temperate regions, *Remote*
696 *Sensing of Environment* 177 (2016) 248–264.
- 697 B. Cao, Q. Liu, Y. Du, J.-L. Roujean, J.-P. Gastellu-Etchegorry, I. F. Trigo, W. Zhan,
698 Y. Yu, J. Cheng, F. Jacob, et al., A review of earth surface thermal radiation direc-
699 tionality observing and modeling: Historical development, current status and per-
700 spectives, *Remote Sensing of Environment* 232 (2019) 111304.
- 701 Z. Bian, J.-L. Roujean, J.-P. Lagouarde, B. Cao, H. Li, Y. Du, Q. Liu, Q. Xiao, Q. Liu,
702 A semi-empirical approach for modeling the vegetation thermal infrared directional
703 anisotropy of canopies based on using vegetation indices, *ISPRS Journal of Pho-*
704 *togrammetry and Remote Sensing* 160 (2020) 136–148. URL: [http://dx.doi.](http://dx.doi.org/10.1016/j.isprsjprs.2019.12.004)
705 [org/10.1016/j.isprsjprs.2019.12.004](http://dx.doi.org/10.1016/j.isprsjprs.2019.12.004). doi:10.1016/j.isprsjprs.2019.
706 [12.004](http://dx.doi.org/10.1016/j.isprsjprs.2019.12.004).
- 707 Z. Bian, J. Roujean, T. Fan, Y. Dong, T. Hu, B. Cao, H. Li, Y. Du, Q. Xiao,
708 Q. Liu, An angular normalization method for temperature vegetation dryness in-
709 dex (tvd) in monitoring agricultural drought, *Remote Sensing of Environment*
710 284 (2023) 113330. URL: <http://dx.doi.org/10.1016/j.rse.2022.113330>.
711 doi:10.1016/j.rse.2022.113330.

- 712 P. Yang, E. Prikaziuk, W. Verhoef, C. van der Tol, Scope 2.0: a model to simulate veg-
713 etated land surface fluxes and satellite signals, *Geoscientific Model Development* 14
714 (2021) 4697–4712. URL: <http://dx.doi.org/10.5194/gmd-14-4697-2021>.
715 doi:10.5194/gmd-14-4697-2021.
- 716 J. Gastellu-Etchegorry, Modeling radiative transfer in heterogeneous 3-d veg-
717 etation canopies, *Remote Sensing of Environment* 58 (1996) 131–156.
718 URL: [http://dx.doi.org/10.1016/0034-4257\(95\)00253-7](http://dx.doi.org/10.1016/0034-4257(95)00253-7). doi:10.1016/
719 0034-4257(95)00253-7.
- 720 J.-P. Gastellu-Etchegorry, N. Lauret, T. Yin, L. Landier, A. Kallel, Z. Malenovsky,
721 A. A. Bitar, J. Aval, S. Benhmida, J. Qi, G. Medjdoub, J. Guilleux, E. Chavanon,
722 B. Cook, D. Morton, N. Chrysoulakis, Z. Mitraka, Dart: Recent advances in remote
723 sensing data modeling with atmosphere, polarization, and chlorophyll fluorescence,
724 *IEEE Journal of Selected Topics in Applied Earth Observations and Remote Sensing* 10 (2017) 2640–2649. URL: [http://dx.doi.org/10.1109/jstars.2017.](http://dx.doi.org/10.1109/jstars.2017.2685528)
725 [2685528](http://dx.doi.org/10.1109/jstars.2017.2685528). doi:10.1109/jstars.2017.2685528.
726
- 727 S. L. Ermida, I. F. Trigo, C. C. DaCamara, J.-L. Roujean, Assessing
728 the potential of parametric models to correct directional effects on local to
729 global remotely sensed LST, *Remote Sensing of Environment* 209 (2018)
730 410–422. URL: [https://www.sciencedirect.com/science/article/pii/](https://www.sciencedirect.com/science/article/pii/S0034425718300798)
731 [S0034425718300798](https://www.sciencedirect.com/science/article/pii/S0034425718300798). doi:10.1016/j.rse.2018.02.066.
- 732 A. Pinheiro, J. Privette, P. Guillevic, Modeling the observed angular anisotropy of
733 land surface temperature in a savanna, *IEEE Transactions on Geoscience and Re-*
734 *remote Sensing* 44 (2006) 1036–1047. URL: [http://dx.doi.org/10.1109/tgrs.](http://dx.doi.org/10.1109/tgrs.2005.863827)
735 [2005.863827](http://dx.doi.org/10.1109/tgrs.2005.863827). doi:10.1109/tgrs.2005.863827.
- 736 Z. Bian, B. Cao, H. Li, Y. Du, J.-P. Lagouarde, Q. Xiao, Q. Liu, An analytical four-
737 component directional brightness temperature model for crop and forest canopies,
738 *Remote Sensing of Environment* 209 (2018) 731–746. URL: [http://dx.doi.org/](http://dx.doi.org/10.1016/j.rse.2018.03.010)
739 [10.1016/j.rse.2018.03.010](http://dx.doi.org/10.1016/j.rse.2018.03.010). doi:10.1016/j.rse.2018.03.010.

- 740 B. Cao, J.-P. Gastellu-Etchegorry, Y. Du, H. Li, Z. Bian, T. Hu, W. Fan, Q. Xiao, Q. Liu,
741 Evaluation of four kernel-driven models in the thermal infrared band, *IEEE Transac-*
742 *tions on Geoscience and Remote Sensing* 57 (2019) 5456–5475. URL: [http://dx.](http://dx.doi.org/10.1109/TGRS.2019.2899600)
743 [doi.org/10.1109/TGRS.2019.2899600](http://dx.doi.org/10.1109/TGRS.2019.2899600). doi:10.1109/tgrs.2019.2899600.
- 744 C. Duffour, J. P. Lagouarde, J. L. Roujean, A two parameter model to simulate
745 thermal infrared directional effects for remote sensing applications, *Remote Sens-*
746 *ing of Environment* 186 (2016) 250–261. URL: [https://www.sciencedirect.](https://www.sciencedirect.com/science/article/pii/S0034425716303157)
747 [com/science/article/pii/S0034425716303157](https://www.sciencedirect.com/science/article/pii/S0034425716303157). doi:10.1016/j.rse.2016.
748 08.012.
- 749 K. Y. Vinnikov, Y. Yu, M. D. Goldberg, D. Tarpley, P. Romanov, I. Laszlo, M. Chen,
750 Angular anisotropy of satellite observations of land surface temperature, *Geophys-*
751 *ical Research Letters* 39 (2012) n/a–n/a. URL: [http://dx.doi.org/10.1029/](http://dx.doi.org/10.1029/2012gl1054059)
752 [2012gl1054059](http://dx.doi.org/10.1029/2012gl1054059). doi:10.1029/2012gl1054059.
- 753 P. C. Guillevic, A. Bork-Unkelbach, F. M. Gottsche, G. Hulley, J.-P. Gastellu-
754 Etchegorry, F. S. Olesen, J. L. Privette, Directional viewing effects on
755 satellite land surface temperature products over sparse vegetation canopies-
756 a multisensor analysis, *IEEE Geoscience and Remote Sensing Letters* 10
757 (2013) 1464–1468. URL: <http://dx.doi.org/10.1109/LGRS.2013.2260319>.
758 doi:10.1109/lgrs.2013.2260319.
- 759 H. Ren, R. Liu, G. Yan, X. Mu, Z.-L. Li, F. Nerry, Q. Liu, Angular normaliza-
760 tion of land surface temperature and emissivity using multiangular middle and
761 thermal infrared data, *IEEE Transactions on Geoscience and Remote Sensing* 52
762 (2014) 4913–4931. URL: <http://dx.doi.org/10.1109/tgrs.2013.2285924>.
763 doi:10.1109/tgrs.2013.2285924.
- 764 J. B. Fisher, B. Lee, A. J. Purdy, G. H. Halverson, M. B. Dohlen, K. Cawse-Nicholson,
765 A. Wang, R. G. Anderson, B. Aragon, M. A. Arain, et al., Ecostress: Nasa’s next
766 generation mission to measure evapotranspiration from the international space sta-
767 tion, *Water Resources Research* 56 (2020) e2019WR026058.

- 768 G. Hulley, S. Hook, Ecostress level-2 1st and emissivity algorithm theoretical basis
769 document (atbd)(no. jpl d-94643), Jet Propulsion Laboratory, California Institute of
770 Technology (2018).
- 771 D. Roy, M. Wulder, T. Loveland, W. C.E., R. Allen, M. Anderson, D. Helder, J. Irons,
772 D. Johnson, R. Kennedy, T. Scambos, C. Schaaf, J. Schott, Y. Sheng, E. Vermote,
773 A. Belward, R. Bindschadler, W. Cohen, F. Gao, J. Hipple, P. Hostert, J. Huntington,
774 C. Justice, A. Kilic, V. Kovalskyy, Z. Lee, L. Lyburner, J. Masek, J. McCorkel,
775 Y. Shuai, R. Trezza, J. Vogelmann, R. Wynne, Z. Zhu, Landsat-8: Science and
776 product vision for terrestrial global change research, *Remote Sensing of Environ-*
777 *ment* 145 (2014) 154–172. URL: [http://dx.doi.org/10.1016/j.rse.2014.](http://dx.doi.org/10.1016/j.rse.2014.02.001)
778 [02.001](http://dx.doi.org/10.1016/j.rse.2014.02.001). doi:10.1016/j.rse.2014.02.001.
- 779 S. J. Hook, J. J. Myers, K. J. Thome, M. Fitzgerald, A. B. Kahle, The modis/aster
780 airborne simulator (master)—a new instrument for earth science studies, *Remote*
781 *Sensing of Environment* 76 (2001) 93–102.
- 782 G. C. Hulley, S. J. Hook, E. Abbott, N. Malakar, T. Islam, M. Abrams, The aster global
783 emissivity dataset (aster ged): Mapping earth’s emissivity at 100 meter spatial scale,
784 *Geophysical Research Letters* 42 (2015) 7966–7976. URL: [http://dx.doi.org/](http://dx.doi.org/10.1002/2015GL065564)
785 [10.1002/2015GL065564](http://dx.doi.org/10.1002/2015GL065564). doi:10.1002/2015g1065564.
- 786 A. Berk, P. Conforti, R. Kennett, T. Perkins, F. Hawes, J. van den Bosch, Modtran6: a
787 major upgrade of the modtran radiative transfer code, in: *Algorithms and Technolo-*
788 *gies for Multispectral, Hyperspectral, and Ultraspectral Imagery XX*, 2014, p. nil.
789 URL: <http://dx.doi.org/10.1117/12.2050433>. doi:10.1117/12.2050433.
- 790 R. Gelaro, W. McCarty, M. J. Suárez, R. Todling, A. Molod, L. Takacs, C. A. Ran-
791 dles, A. Darmenov, M. G. Bosilovich, R. Reichle, K. Wargan, L. Coy, R. Cul-
792 lather, C. Draper, S. Akella, V. Buchard, A. Conaty, A. M. da Silva, W. Gu, G.-
793 K. Kim, R. Koster, R. Lucchesi, D. Merkova, J. E. Nielsen, G. Partyka, S. Paw-
794 son, W. Putman, M. Rienecker, S. D. Schubert, M. Sienkiewicz, B. Zhao, The
795 modern-era retrospective analysis for research and applications, version 2 (merra-2),

796 Journal of Climate 30 (2017) 5419–5454. URL: <http://dx.doi.org/10.1175/>
797 [JCLI-D-16-0758.1](http://dx.doi.org/10.1175/JCLI-D-16-0758.1). doi:10.1175/jcli-d-16-0758.1.

798 N. K. Malakar, G. C. Hulley, S. J. Hook, K. Laraby, M. Cook, J. R. Schott, An
799 operational land surface temperature product for landsat thermal data: Methodol-
800 ogy and validation, IEEE Transactions on Geoscience and Remote Sensing 56
801 (2018) 5717–5735. URL: <http://dx.doi.org/10.1109/TGRS.2018.2824828>.
802 doi:10.1109/tgrs.2018.2824828.

803 S. J. Hook, et al., HypsIRI Level-2 Thermal Infrared (TIR) land surface temperature
804 and emissivity algorithm theoretical basis document., Technical Report, Pasadena,
805 CA: Jet Propulsion Laboratory, National Aeronautics and Space . . . , 2011.

806 D. Hoese, P. Lahtinen, M. Raspaud, W. Roberts, Lavergne, S. Bot, G. Holl,
807 S. Finkensieper, G. Ghiggi, A. Dybbroe, X. Zhang, M. Itkin, A. Meraner,
808 BENRO, A. Valentino, Nina, L. Ørum Rasmussen, lorenzo clementi, M. Val-
809 gur, D. Rykov, A. Brammer, B. Hawkins, F. Pinault, storpipfugl, owenlittlejohns,
810 A. R. P. Morena, B. Couwenberg, B. Esse, pytroll/pyresample: Version 1.26.0 post
811 0, 2022. URL: <https://doi.org/10.5281/zenodo.7358887>. doi:10.5281/
812 [zenodo.7358887](https://doi.org/10.5281/zenodo.7358887).

813 L. Su, X. Li, M. Friedl, A. Strahler, X. Gu, Kernel-driven model of effective directional
814 emissivity for non-isothermal surfaces, Progress in Natural Science 12 (2002) 603–
815 607.

816 J.-P. Lagouarde, M. Irvine, Directional anisotropy in thermal infrared measurements
817 over toulouse city centre during the capitoul measurement campaigns: First results,
818 Meteorology and Atmospheric Physics 102 (2008) 173–185. URL: [http://dx.](http://dx.doi.org/10.1007/s00703-008-0325-4)
819 [doi.org/10.1007/s00703-008-0325-4](http://dx.doi.org/10.1007/s00703-008-0325-4). doi:10.1007/s00703-008-0325-4.

820 P. Virtanen, R. Gommers, T. E. Oliphant, M. Haberland, T. Reddy, D. Cournapeau,
821 E. Burovski, P. Peterson, W. Weckesser, J. Bright, S. J. van der Walt, M. Brett,
822 J. Wilson, K. J. Millman, N. Mayorov, A. R. J. Nelson, E. Jones, R. Kern, E. Larson,
823 C. J. Carey, Í. Polat, Y. Feng, E. W. Moore, J. VanderPlas, D. Laxalde, J. Perktold,

824 R. Cimrman, I. Henriksen, E. A. Quintero, C. R. Harris, A. M. Archibald, A. H.
825 Ribeiro, F. Pedregosa, P. van Mulbregt, A. Vijaykumar, A. P. Bardelli, A. Roth-
826 berg, A. Hilboll, A. Kloeckner, A. Scopatz, A. Lee, A. Rokem, C. N. Woods,
827 C. Fulton, C. Masson, C. Häggström, C. Fitzgerald, D. A. Nicholson, D. R. Hagen,
828 D. V. Pasechnik, E. Olivetti, E. Martin, E. Wieser, F. Silva, F. Lenders, F. Wilhelm,
829 G. Young, G. A. Price, G.-L. Ingold, G. E. Allen, G. R. Lee, H. Audren, I. Probst,
830 J. P. Dietrich, J. Silterra, J. T. Webber, J. Slavič, J. Nothman, J. Buchner, J. Kulick,
831 J. L. Schönberger, J. V. de Miranda Cardoso, J. Reimer, J. Harrington, J. L. C. Ro-
832 dríguez, J. Nunez-Iglesias, J. Kuczynski, K. Tritz, M. Thoma, M. Newville, M. Küm-
833 merer, M. Bolingbroke, M. Tartre, M. Pak, N. J. Smith, N. Nowaczyk, N. Shebanov,
834 O. Pavlyk, P. A. Brodtkorb, P. Lee, R. T. McGibbon, R. Feldbauer, S. Lewis, S. Ty-
835 gier, S. Sievert, S. Vigna, S. Peterson, S. More, T. Pudlik, T. Oshima, T. J. Pin-
836 gel, T. P. Robitaille, T. Spura, T. R. Jones, T. Cera, T. Leslie, T. Zito, T. Krauss,
837 U. Upadhyay, Y. O. Halchenko, Y. Vázquez-Baeza, S. . Contributors, Scipy
838 1.0: Fundamental algorithms for scientific computing in python, Nature Methods
839 17 (2020) 261–272. URL: <http://dx.doi.org/10.1038/s41592-019-0686-2>.
840 doi:10.1038/s41592-019-0686-2.

841 N.-E. Tsendbazar, A. Tarko, L. Li, M. Herold, M. Lesiv, S. Fritz, V. Maus, Coper-
842 nicus Global Land Service: Land Cover 100m: version 3 Globe 2015-2019:
843 Validation Report, 2021. URL: <https://doi.org/10.5281/zenodo.4723975>.
844 doi:10.5281/zenodo.4723975.

845 F. Kriegler, W. Malila, R. Nalepka, W. Richardson, Preprocessing transformations and
846 their effects on multispectral recognition, Remote sensing of environment, VI (1969)
847 97.

848 R. Niclòs, J. Puchades, C. Coll, M. J. Barberà, L. Pérez-Planells, J. A. Valiente, J. M.
849 Sánchez, Evaluation of landsat-8 tirs data recalibrations and land surface temper-
850 ature split-window algorithms over a homogeneous crop area with different pheno-
851 logical land covers, ISPRS Journal of Photogrammetry and Remote Sensing 174
852 (2021) 237–253. URL: [http://dx.doi.org/10.1016/j.isprsjprs.2021.02.](http://dx.doi.org/10.1016/j.isprsjprs.2021.02.005)
853 [005](http://dx.doi.org/10.1016/j.isprsjprs.2021.02.005). doi:10.1016/j.isprsjprs.2021.02.005.

854 D. Phiri, M. Simwanda, S. Salekin, V. R. Nyirenda, Y. Murayama, M. Ranagalage,
855 Sentinel-2 data for land cover/use mapping: A review, *Remote Sensing* 12 (2020)
856 2291.

857 J.-P. Lagouarde, A. Hénon, B. Kurz, P. Moreau, M. Irvine, J. Voogt, P. Mestayer, Mod-
858 elling daytime thermal infrared directional anisotropy over toulouse city centre, *Re-
859 mote Sensing of Environment* 114 (2010) 87–105. URL: [http://dx.doi.org/10.](http://dx.doi.org/10.1016/j.rse.2009.08.012)
860 [1016/j.rse.2009.08.012](http://dx.doi.org/10.1016/j.rse.2009.08.012). doi:10.1016/j.rse.2009.08.012.

861 L. Jiang, W. Zhan, L. Hu, F. Huang, F. Hong, Z. Liu, J. Lai, C. Wang, Assessment
862 of different kernel-driven models for daytime urban thermal radiation directionality
863 simulation, *Remote Sensing of Environment* 263 (2021) 112562. URL: [http://dx.](http://dx.doi.org/10.1016/j.rse.2021.112562)
864 [doi.org/10.1016/j.rse.2021.112562](http://dx.doi.org/10.1016/j.rse.2021.112562). doi:10.1016/j.rse.2021.112562.

865 J. Michel, O. Hagolle, S. J. Hook, J.-L. Roujean, P. Gamet, Master and Landsat-8
866 simultaneous acquisition datacubes for the quantification of directional anisotropy
867 in Thermal Infra-Red domain, 2023. URL: [https://doi.org/10.5281/zenodo.](https://doi.org/10.5281/zenodo.7757028)
868 [7757028](https://doi.org/10.5281/zenodo.7757028). doi:10.5281/zenodo.7757028.

869 **List of Figures**

870	1	Location of the 12 MASTER tracks that have been matched to near simultaneous Landsat-8 acquisitions	8
871			
872	2	Detailed view of the overlapping MASTER tracks and Landsat-8 near simultaneous acquisitions. When two Landsat-8 images match a given track, the first image (a) is displayed in red and second image (b) in blue.	9
873			
874			
875	3	Spectral Sensitivity Response of Landsat-8 and MASTER overlapping Thermal Infra-Red spectral bands	12
876			
877	4	Maps of SBT difference (Landsat-8 - MASTER), corrected of the bias computed in table 6 for all tracks (negative values are in red and mean that MASTER is warmer than Landsat-8)	21
878			
879			

880	5	SBT difference (Landsat-8 - MASTER) with respect to angular distance from MASTER to hotspot and from MASTER to Landsat-8, corrected of the bias computed in table 6 (negative values are in red and mean that MASTER is warmer than Landsat-8)	22
881			
882			
883			
884	6	SBT difference (Landsat-8 - MASTER) with respect to MASTER view zenith and azimuth, corrected of the bias computed in table 6. Average sun position is marked by an orange star. (negative values are in red and mean that MASTER is warmer than Landsat-8)	23
885			
886			
887			
888	7	SBT difference, corrected of the bias computed in table 6, with respect to MASTER signed view zenith angle (positive angles are to the east, negative to the west). The solid red line indicates the mean values, the red dashed line indicates mean ± 1 standard deviation. Blue dotted lines indicate TRISHNA and SBG FOV.	24
889			
890			
891			
892			
893	8	Mean \pm standard-deviation of unbiased SBT difference with respect to MASTER signed view zenith angle for the major land-cover classes (> 15%) of each land cover classes as highlighted in table 5.	27
894			
895			
896	9	Least-Square fitting of the five TIR directional models from table 3 on SBT differences. Vertical axis represent the percentage of variation of SBT between Landsat-8 (considered as Nadir) and MASTER. In this figure, each model is fitted separately on each track.	28
897			
898			
899			
900	10	Corrected SBT versus signed VZA for raw and model-corrected SBT, for 5 tracks with high directional effects amplitudes. Blue dashed lines indicate Trishna FOV.	31
901			
902			
903	11	Least-Square fitting of the five TIR directional models from table 3 on SBT differences. Vertical axis represent the percentage of variation of SBT between Landsat-8 (considered as Nadir) and MASTER. In this figure, each model is jointly fitted on all tracks.	33
904			
905			
906			
907	12	Corrected SBT versus signed VZA for raw and model-corrected SBT, using models jointly fitted on all tracks, for 5 tracks with high directional effects amplitudes. Blue dashed lines indicate TRISHNAP FOV.	34
908			
909			

910	13	Polar plot of the different models, jointly fitted on all tracks, using av-	
911		erage solar angles of track (12). Sun position is indicated by an orange	
912		star mark.	35